ELSEVIER

Journal of Molecular Catalysis A: Chemical 162 (2000) 463–492

JOURNAL OF MOLECULAR CATALYSIS A: CHEMICAL

www.elsevier.com/locate/molcata

Molybdenum oxide based partial oxidation catalyst: 1. Thermally induced oxygen deficiency, elemental and structural heterogeneity and the relation to catalytic performance

G. Mestl [*], Ch. Linsmeier [1], R. Gottschall [2], M. Dieterle, J. Find [3], D. Herein [4], J. Jäger, Y. Uchida, R. Schlögl

Fritz-Haber-Institut der Max-Planck-Gesellschaft, Abt. Anorganische Chemie, Faradayweg 4-6, 14195 Berlin, Germany

Dedicated to Prof. Helmut Knözinger in honor of his 65th birthday.

Abstract

A mixed oxide catalyst containing Mo, V, and W was used for the partial oxidation of methanol. The relation between the structure and the degree of reduction of this mixed oxide catalyst and its catalytic performance was investigated by scanning electron microscopy (SEM), transmission electron microscopy (TEM), energy dispersive X-ray (EDX), Rutherford backscattering (RBS), XPS, ion scattering spectroscopy (ISS), UPS, X-ray diffraction (XRD) and Raman microspectroscopy. Thermal activation of the MoVW mixed oxide led to an increase in the methanol conversion by a factor of 3 and an increase in selectivity to formaldehyde from 66% to 80%. SEM–EDX characterization of the untreated catalyst revealed the presence of at least two different phases in the sample on a micron range, one with a high V concentration, and another with all three metals present. TEM–EDX showed a homogeneous element distribution in the submicron regime. The thermally activated mixed oxide revealed an inhomogeneous element distribution in the micron and submicron regime as shown by SEM–EDX and TEM–EDX. The activation led to a reduction of the bulk oxide as determined by RBS and its surface as shown by XPS, ISS, and UPS. The formation of Mo^{4+} and V^{4+} centers was detected at the catalyst surface upon thermal activation. XRD of the starting material showed the presence of nanocrystalline material which was identified as being a mixture of a majority of Mo_5O_{14} and a minority of MoO_3-type MoVW oxides. Confocal Raman microspectroscopy confirmed the presence of two different components. The major component could be identified as amorphous Mo_5O_{14}-type MoVW mixed oxide. The second, minor component was similar to an amorphous MoO_3-type MoVW oxide. XRD showed that the thermally activated mixed oxide consisted of a mixture of a majority of crystalline Mo_5O_{14}-type oxide and of small amounts of crystalline MoO_3-type and MoO_2-type oxides. The Raman spectrum of the Mo_5O_{14}-type phase could be identified by statistical data evaluation of 1000 spectra and by comparison with the XRD result. Raman microscopy confirmed the

[*] Corresponding author. Tel.: +49-30-8413-4440; fax: +49-30-8413-4401.
E-mail address: mestl@fhi-berlin.mpg.de (G. Mestl).
[1] Max-Planck-Institut für Plasmaphysik, Boltzmannstr. 2, 85748 Garching, Germany.
[2] Inst. f. Anorg. and Analyt. Chemie, Albert-Ludwigs-Universität, Albertstr. 21 D-79104 Freiburg i. Br., Germany.
[3] Department of Chemical Engineering, Worcester Polytechnical Institute, 100 Institute Road, Worcester, MA 01609-2280, USA.
[4] Inst. Anorg. Analyt. Chemie, Technische Universität Berlin, Straße des 17. Juni 135, D-10623 Berlin, Germany.

1381-1169/00/$ - see front matter
PII: S1381-1169(00)00340-X

presence of a minority of MoO_3- and MoO_2-type oxide. The formation of Mo_5O_{14}-type oxide upon loss of oxygen is discussed with respect to the remarkable increase in the catalytic activity and selectivity.

Keywords: Mixed oxide catalyst; Partial oxidation; Catalytic performance

1. Introduction

Catalytic selective oxidation reactions belong to the most important industrial processes. About one quarter of the value produced worldwide via catalytic reactions stems from partial oxidation reactions, and hence, they considerably contribute to the gross national products of industrialized countries [1]. Thus, it is highly important to further develop not only the performance of such industrial processes but also the fundamental understanding of such multielement and multiphase catalysts, e.g. the role of each phase and their interaction under catalytic action. This information is prerequisite for future material science tailoring of molecularly defined selective catalysts.

The Mars–van Krevelen mechanism is generally accepted for selective partial oxidation reactions and describes the role of the so-called, active "lattice" oxygen for selective partial oxidations [2]. The adsorption of alkenes is suggested to occur at the (100) surface of MoO_3 on coordinatively unsaturated Mo sites under the formation of an allylic intermediate [3,4]. The second reaction step, the nucleophilic oxygen insertion, is thought to occur on the (010) surface via the formation of a σ bond between the "lattice oxygen" and the allylic intermediate. The nucleophilic oxygen species is then inserted into the hydrocarbon to give the oxygenated product, which desorbs, leaving an oxygen vacancy at the catalyst surface [5]. This oxygen vacancy is reoxidized in the last step of the catalytic cycle and it is suggested that this occurs via oxygen bulk diffusion. However, the actual nature of the "lattice" oxygen is still not fully unraveled, and it is still under debate which of the different possible metal–oxygen species actually take part in the oxygen insertion reaction [3,6]. From this accepted model, it can be assumed that the surface oxygen defects generated during catalysis may be replenished either by surface oxygen diffusion, by oxygen diffusion through the surface near layer or by oxygen bulk diffusion (Scheme 1). It may further be anticipated that each of these three layers has a different chemical composition and structure. Moreover, this three-layer model may still be too simple and the actual catalyst may exhibit spatial differences in composition and structure. It may be anticipated that oxygen diffusivities are affected by the elemental compositions and the geometric structures of the catalyst phases. The real metal–oxygen stoichiometry and defect structure of molybdenum oxides thus may play an important role in selective partial oxidation reactions. It can be assumed that the degree of reduction, and hence, the presence of reduced surface metal centers, strongly affects the adsorption properties of hydrocarbons, and the C–H bond activation. The electronic properties of reduced molybdenum oxides, i.e. high electron density at the surface, may effect the oxygen activation.

X-ray diffraction (XRD) and transmission electron microscopy (TEM) literature provides information about structural changes of molybdenum oxides as function of their degree of reduction [7–23]. The MoO_3 crystal structure (Scheme 2) is built up by chains of MoO_4 tetrahedra running in *c*-direction. The chains are condensed to layers in the *ac* plane [24]. The loss of oxygen from the MoO_3 lattice was first suggested to lead to an Mo–Mo bond across the anion vacancy [25,26]. These defects are mobile and order to extended shear defect structures upon further reduction [13,27–29]. A whole series of oxygen deficient structures was identified between MoO_3 and MoO_2 (Table 1) [17–19,21,23,25].

The basis of partial oxidation catalysts often is molybdenum oxide mixed with vanadium and tungsten oxides [30]. For example, the best catalytic properties for the selective oxidation of acrolein were reported for a mixture of MoO_3 with 7–15% V_2O_4, which was suggested to exhibit the Mo_3VO_{11}-structure with the formal stoichiometry of $Mo_{0.75}V_{0.25}O_{2.75}$ [30–32]. These MoVW mixed oxide catalysts have been improved over the years by

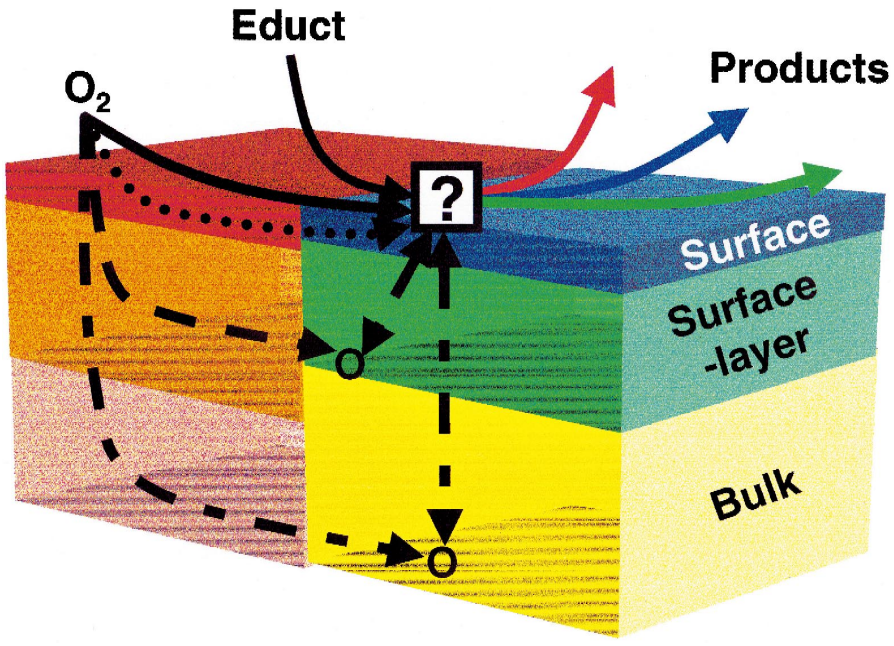

Scheme 1. Schematic drawing of different possible oxygen diffusion pathways in multicomponent, multiphase partial oxidation catalysts.

adding more and more promotors [33–42]. Hence, it has become increasingly more difficult to fully understand the role of each element and each phase present in such multielement partial oxidation catalysts on an atomic level.

Previous XRD and HRTEM results on the MoVW mixed oxide catalyst of a formal stoichiometry of $Mo_9V_3W_{1.2}O_x$ revealed an amorphous state being built by Mo_5O_{14}-type subunits [43]. The crystallization of an Mo_5O_{14}-type phase was observed after

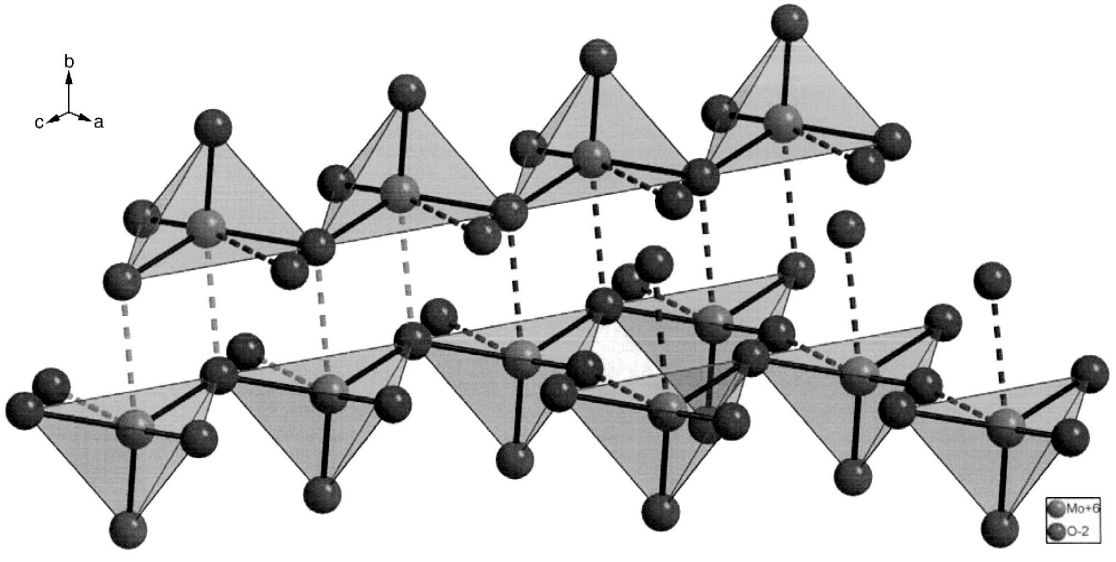

Scheme 2. Schematic drawing of the MoO_3 crystal lattice showing the four-fold, distorted tetrahedral oxygen coordination sphere around Mo^{6+}.

Table 1

HRTEM							
Sum formula	Mo_8O_{23}	Mo_9O_{26}	$Mo_{10}O_{29}$	$Mo_{11}O_{32}$	$Mo_{12}O_{35}$	$Mo_{14}O_{41}$	
Stoichiometry	2.875	2.888	2.9	2.909	2.916	2.928	
XRD							
Sum formula	MoO_2	Mo_4O_{11}	$Mo_{17}O_{47}$	Mo_5O_{14}	Mo_8O_{23}	$Mo_{18}O_{52}$; Mo_9O_{26}	MoO_3
Stoichiometry	2	2.75	2.765	2.8	2.875	2.888	3

thermal activation in air [43]. Kihlborg [16] and Yamazoe and Kihlborg [44] described this oxide to crystallize in the space group 4/mmm with an orthorhombic unit cell of the dimensions $a = b = 4.599$ nm and $c = 393.7$ pm which is characterized by a superstructure along the *c*-axis. The structure is built up by distorted four-, six- and seven-fold (pentagonal bipyramids) Mo coordination polyhedra being mutually connected by sharing corners or edges and stacked along *a*. The Mo−O distances of the six-fold coordination range between 164 and 173 pm and between 228 and 237 pm, those of the pentagonal bipyramid are 177, 181, 219 and 223 pm (Scheme 3, lower sketch). The structure is disordered in the *ab* plane with the Mo atoms of the pentagonal bipyramid randomly distributed above and below this plane [44], and crystallizes in bundles of small needles. Mo_5O_{14} is metastable with respect to MoO_2 and MoO_3 and slowly decomposes at its formation temperature [16].

Mixed MoVW oxides with the Mo_5O_{14} structure can be synthesized from MoO_3, WO_3, and V_2O_5 by sintering. Their stoichiometry was described to be $(Mo_{0.92}V_{0.08})_5O_{14}$ or $(Mo_{0.75}W_{0.25})_5O_{14}$) [45–47], respectively, which is close to that of technical catalysts. An increased stability of this *θ*-molybdenum oxide was observed for vanadium concentrations between 2 and 12 cation % [45,46]. The Mo_5O_{14} structure tolerates the incorporation of Nb and Ta [44,48], and Ti, too [49,50]. For example, the amount of incorporated Ta [44] compares with the W concentration in the presently investigated mixed oxide catalyst. Vanadium seems to be statistically distributed in the *θ*-molybdenum oxide [47], whereas Ta is exclusively located in the pentagonal bipyramid [44].

These pentagonal bipyramids are also found in $Mo_{17}O_{47}$ [12,13], being similar to $W_{18}O_{49}$ [12,51,52]. The cylindrical shear structural motif is the general relation between Mo_5O_{14}, $Mo_{17}O_{47}$, $Nb_{16}W_{18}O_{94}$, $Bi_6Nb_{34}O_{94}$, and tetragonal tungsten bronzes [53]. The cylindrical shear mechanism can be understood as the rotation of an Mo_4O_{20} subunit within an MoO_3-layer giving rise to uncounted possibilities of disorder, intergrowth, and nonstoichiometry.

Each of these crystallographic structures in principle may expose different metal–oxygen groups and types of oxygen vacancies at their surfaces. The actual nature and role of these different possible surface sites for selective partial oxidation reactions are not understood yet, although often discussed [3–6,54]. Due to the relevance of oxygen defects for selective oxidation, the effect of thermal activation on the catalytic activity of an MoVW mixed oxide catalyst was investigated. Because methanol is very reactive and because the possible reaction products are linked to different reaction channels [55–58], the conversion of methanol to formaldehyde was used as a test reaction to investigate the catalytic properties of the mixed oxide. Pure "MoO_3" catalysts exhibit high selectivities to formaldehyde [59]. The rate-determining step was identified to be the hydrogen abstraction from the methyl group [60]. Mo=O double bonds were suggested to be active for the formaldehyde formation [55–58], while bridged Mo−O−Mo sites lead to dimethyl ether [58]. In this respect, it is interesting to note that the oxygen exchange capabilities of the different Mo−O bonds in MoO_3 depend on the Mo−O bond order [60,61].

In the present study, the structure, degree of reduction, and elemental composition of a technical catalyst was investigated. Changes in the redox properties, elemental compositions, and structure of the catalyst induced by the thermal activation are discussed with respect to the altered catalytic performance.

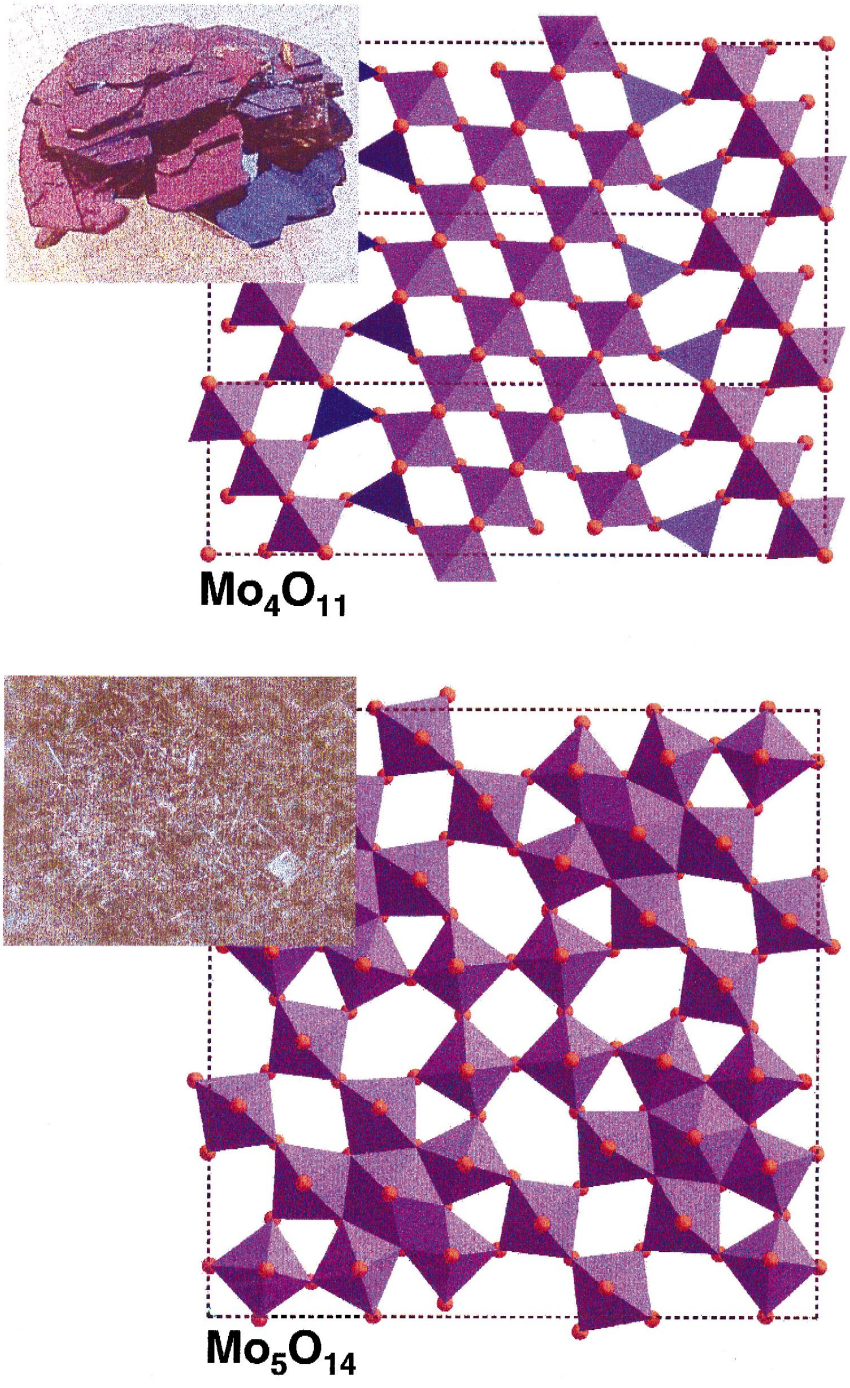

Scheme 3. Schematic drawing of the Mo_4O_{11} (upper sketch) and Mo_5O_{14} (lower sketch) crystal lattices.

2. Experimental

2.1. Catalyst preparation

The catalyst was prepared by spray drying aqueous solutions of the respective ammonium salts to give the formal composition of $Mo_{0.68}V_{0.23}W_{0.09}O_x$ followed by calcination at 700 K in a 5% O_2/95% N_2 mixture. One part of this batch was modified by heating in an inert gas stream of 150 ml/min at 813 K for 2 h. This activation was characterized by thermogravimetry (TG)–DTA with a SEIKO microbalance. An ion–molecule-reaction mass spectrometer (IMR-MS 100, Atomika) was used to detect the desorbing gases. Xe^+ and Kr^+ ions were used for ionization. The signal intensities were referenced to the signal intensity of a defined flow of benzene added at the reactor outlet. The error in quantification due to the non-linear behavior of the ionization cross-sections are considerable for components like H_2O or MeOH, which are partly protonated in the octupole of the IMR-MS by secondary reactions. In order to reduce these problems, H_2O had been calibrated in the presence of MeOH and vice versa but still the error is about 20 relative %.

2.2. Catalytic characterization

The catalyst (50 mg, BET surface area 4 m^2/g, average particle size: 10 μm) was diluted with SiC (Aldrich, 500 mg, particle size 5 μm) and placed between quartz wool plugs in a glass tubular flow reactor of 6 mm inner diameter and 300 mm length leading to a catalyst bed length of 15 mm. The reactor dead volume was minimized to 1.5 ml by a glass stick inserted downstream of the catalyst bed. A flow of 5 ml/min N_2 was fed into an evaporator at 298 K to obtain a gas stream saturated with 8 μmol/ml CH_3OH. The default gas flow of O_2 was 2.5 ml/min to get a reactant ratio of MeOH: O_2 = 2.5. An additional flow of N_2 was used to obtain a constant total flow rate of 200 ml/min (space velocity 28 300 h^{-1}). Product analysis was performed by IMR-MS (IMRMS 100, Atomika).

2.3. Scanning electron microscopy (SEM), TEM, and energy dispersive X-ray (EDX) analysis

SEM was conducted with a S 4000 FEG microscope (Hitachi). The acceleration voltage was set to 10 kV, the objective aperture was 30 μm, and the working distance was 10 mm. The samples were suspended in CCl_4, and mounted on Be platelets. EDX was done with a DX 4 analyzer system (EDAX) equipped with a Li-doped Si crystal with a resolution of 140 eV at 5.9 keV, and an acceleration voltage of 15 kV. Adsorption correction was automatically performed, position correction was done by inspection.

TEM was performed on a CM200 FEG microscope (Philips). The acceleration voltage was set to 200 kV. The samples were suspended in CCl_4 and mounted on a carbon foil supported on a Cu net. EDX analysis was done using the DX 4 analyzer system (EDAX) equipped with an Li-doped Si detector with a resolution of 140 eV at 5.9 kV.

2.4. Rutherford backscattering spectroscopy (RBS)

RBS was used for the quantification of the bulk catalyst composition. RBS spectra with different elemental compositions were simulated using the software SIMNRA [62]. According to the simulations, ^1H with an energy of 2 MeV at a scattering angle of 165° has been selected as optimum leading to an information depth of several 10 μm. For quantification, the RBS spectra were first fitted in the high energy region of the W and Mo edges, because concentration changes of 0.01% already led to altered intensities. Rutherford cross-sections were used for V, Mo, and W. A non-Rutherford cross-section was used for O due to the high proton energy. Subsequent fitting runs were carried out with varying V concentrations, while the oxygen concentration gave the difference to 100%. The V and O amounts were varied until an optimum fit was reached. The confidence levels of the metal quantification gave standard deviations of 0.01% for W and Mo, and 0.16% for V, respectively, while the error of the oxygen quantification is 0.16% for the untreated mixed oxide. The error in the oxygen determination is reduced to 0.04% for the thermally treated mixed oxide.

2.5. Photoelectron spectroscopy

Surface analysis was performed with a combined XPS–UPS–ISS instrument (Leybold–Heraeus) with

an EA 200 hemispherical analyzer at a band pass energy of 48 eV resulting in 1.0 eV resolution. Mg K_α X-ray radiation (150 W) was used. The XPS binding energy scale was calibrated with Au 4f at 84 eV and Cu 2p at 932.7 eV. The data were analyzed using satellite subtraction, Shirley background subtraction, integration using empirical sensitivity factors determined for the instrumental geometry. He I and He II UV radiation was used for UPS with a bandpass energy of 12 and 24 eV, respectively. ISS was performed with He^+ ions at 1 keV and an ion current of 1 nA, giving a fluence of 6×10^{12} ions/cm^2 per scan.

The samples were used as fine powders supported on Au foil sample holders. In case of the mixed oxide after catalysis, the sample had to be separated from SiC and quartz wool by repeatedly suspending it in hexane. The sample still contained SiO_2 and SiC rendering quantitative determination of the oxygen content impossible. Electrostatic charging was compensated using the C 1 s signal of ubiquitous carbon contaminations at 285.0 eV.

2.6. XRD

XRD patterns were recorded on a theta–theta diffractometer (Stoe) in Bragg–Brentano geometry using a scintillation counter detector. Monochromatic (graphite secondary monochromator) Cu K_α (154.18 pm) radiation was used. The measured XRD diffractograms were simulated with the Cerius software package (MSI).

2.7. Raman spectroscopy

Confocal Raman microspectroscopy was conducted with a LabRam B Raman spectrometer (Dilor) equipped with an electrically cooled (-27°C) CCD camera (1152×298 pixel), and a holographic grating of 1800 s/mm. The slit width was set to 200 μm giving a resolution of 2.5 cm^{-1}. The line at 632 nm of a HeNe ion laser (Melles Griot) was used with laser powers of 0.14 and 15 mW at the sample position. Laterally resolved confocal Raman spectra were recorded with an optical microscope (Olympus) of an area of 900 μm^2 giving a set of 1000 Raman spectra per sample. An objective with a magnification of 100 was used giving a spatial resolution about 700 nm. For the low laser power, each spectrum is the sum of two accumulations each integrated for 400 s, for the high laser power each spectrum is the sum of two accumulations each integrated for 1 s. These sets of spectra were statistically evaluated using SIMPLISMA (Simple-to-use interactive self-modeling mixture analysis) [63]. The SIMPLISMA approach allows the determination of the number of components present in a data set and to resolve the data matrix into the linearly independent pure spectra (basis vectors) and a matrix of the concentration coefficients without prior information about the pure spectra or the concentration profiles.

In Fig. 1, characteristic Raman spectra are compared which were recorded with the minimum (spectra a,b) and maximum laser power (spectra c–e). Maximum laser power clearly leads to changing

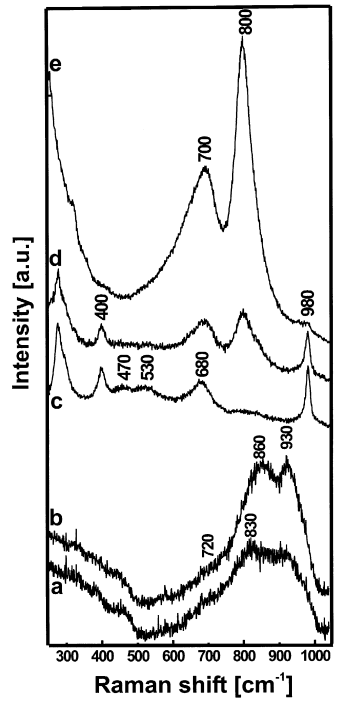

Fig. 1. Spectra (a and b): two representative confocal Raman spectra of untreated MoVW mixed oxide recorded at two different spots (lateral resolution 700 nm) with minimum laser power. Spectra (c to e): Three representative confocal Raman spectra of untreated MoVW mixed oxide recorded at three different spots (lateral res. 700 nm) with maximum laser power.

Raman spectra as compared to those recorded with minimum laser power. Therefore, caution must be taken when recording Raman spectra of such type of catalysts to avoid laser damage. Additionally, it can be seen from the spectral differences that laser damage leads to spatial inhomogeneities in the spectral appearance (spectra c–e).

3. Results and discussion

3.1. Thermal activation of the untreated mixed oxide

Fig. 2 shows the TG analysis (solid line) of the untreated mixed oxide upon thermal activation (section A), during subsequent partial oxidation in methanol: oxygen = 2:1 (section B) and methanol: oxygen = 4:3 (section C), and reoxidation in pure O_2 (section D). The final weight after reoxidation (section D) to MoO_3 (98% of the original value) evidences that the thermal activation (section A) not only led to the loss of H_2O and NH_3 ($\approx$ 2 wt.%), but also to a considerable loss of oxygen ($\approx$ 3 wt.%), as NO and NO_2 which was detected by IMR-MS. The catalytic reaction with methanol (section B) led to a further loss of oxygen, while a subsequent increase in the oxygen partial pressure (section C) first led to a weight gain within 30 min to decrease again later. This transient behavior in section C may be interpreted as the establishment of a steady state of an average oxide stoichiometry below the nominally fully oxidized composition. From the final weight after complete reoxidation, it may be attempted to estimate the stoichiometry of the active catalyst material. From this estimation, it may be suggested that the actual catalyst has a stoichiometry between the only known stable phases in this regime, Mo_8O_{23} and Mo_5O_{14}. It is important to note that the stoichiometry determined by TG analysis can be compared with that determined by RBS (see Section 3.3.2.).

3.2. Temperature programmed reaction spectroscopy (TPRS)

Because the thermal activation in inert gas did not change the BET surface area (it remained constant at 4 m^2/g), the catalytic activities and selectivities of the untreated and the thermally activated catalyst can be compared for identical reactor loadings. In Fig. 3,

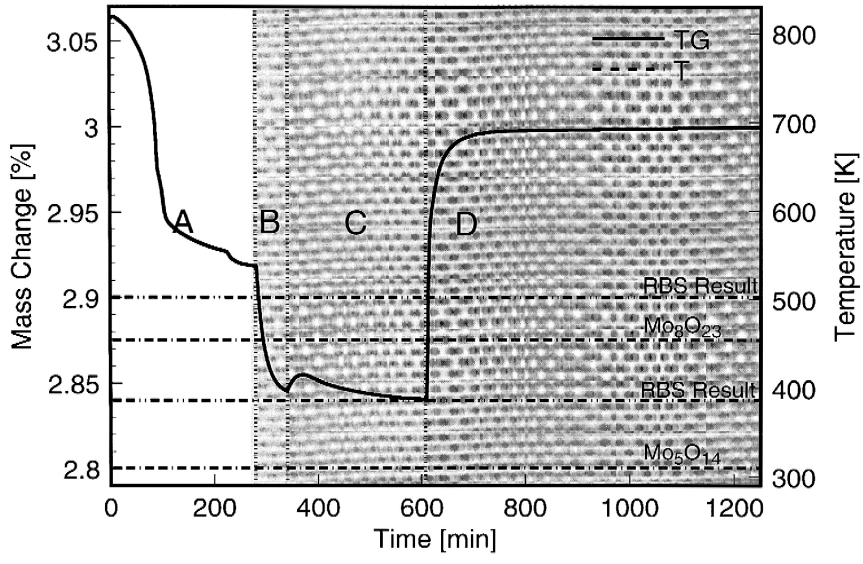

Fig. 2. TG analysis of the weight changes of the untreated mixed oxide upon thermal activation (section A), subsequent partial oxidation in methanol: oxygen = 2:1 (section B) and methanol: oxygen = 4:3 (section C) and complete reoxidation in pure O_2 (section D). Solid line: weight change in percent; Dashed line: temperature program during the experiment.

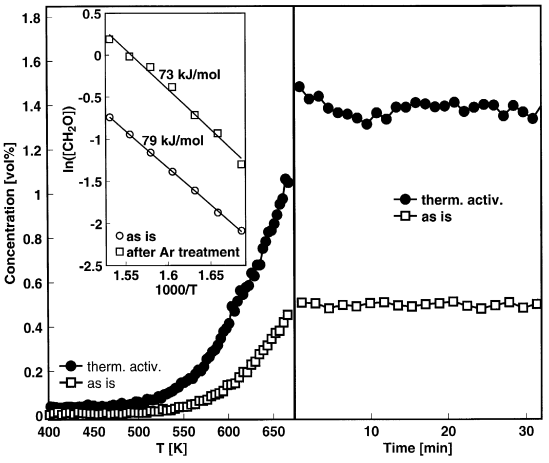

Fig. 3. TPRS from 298 to 673 K (vol.% formaldehyde) together with the isothermal steady state run at 673 K for 50 mg of both, the untreated mixed oxide and the thermally activated catalyst, diluted in 500 mg SiC. The inset shows the activation energies determined over both catalysts, red □: thermally activated mixed oxide, black ○: untreated mixed oxide.

the TPRS is displayed from 298 to 673 K together with the isothermal steady state run for both materials. Beside CO, the main product over the untreated mixed oxide was 0.45 vol.% CH_2O, corresponding to a formaldehyde selectivity of 66% at 31% conversion. Thermal activation increased the CH_2O steady state yield by a factor of 3 as shown in Fig. 2 with a CH_2O selectivity of 80% at 93% conversion. These data may be compared with those of an industrial Fe_2O_3/MoO_3 catalyst reaching 95% to 99% methanol conversion with a formaldehyde selectivity between 91% and 94% [64]. The thermal activation also changed the byproduct spectrum of this reaction. The thermally activated catalyst gave only a small amount of $(CH_3)_2O$ as the byproduct. Thus, according to literature [55–58], it may concluded that two reaction paths are active on the catalyst depending on thermal activation.

$$2CH_3OH + O_2 \Rightarrow 2CH_2O + 2H_2O \quad (\text{site 1: Mo=O}) \quad (1)$$

$$2CH_3{-}OH \Rightarrow CH_3{-}O{-}CH_3 + H_2O \quad (\text{site 2: Mo{-}O{-}Mo}) \quad (2)$$

$$2CH_3OH + 3O_2 \Rightarrow 2CO_2 + 4H_2O \quad (3)$$

The activation energies of the formaldehyde formation over both catalysts were determined between 600 and 663 K (inset of Fig. 3). As CH_2O was the main product and because CO_2 was not detected, the apparent activation energy for the CH_2O formation could be determined to be $E_a = 79$ kJ/mol for the untreated mixed oxide, and $E_a = 73$ kJ/mol for the thermally activated catalyst. The improved activity of the thermally activated catalyst is not attributed to a decreased activation energy but to an increased pre-exponential factor, i.e. an increased number of active sites on the catalyst surface.

An increase of the O_2 partial pressure in the feed by a factor of 3 at 673 K reactor temperature led to a decrease in the CH_2O selectivity from 80% to 61% during 3 h on stream. From the three-fold increase of the stoichiometric oxygen partial pressure, one would expect a much more dramatic decrease in selectivity than the observed 1/4 and the clear detection of CO_2. CO_2, however, was only detected in traces. These observations point to changes in the catalyst material in agreement with the transient behavior seen by the TG experiment.

3.3. Physicochemical characterization

3.3.1. SEM / TEM and EDX analysis

The SEM images reveal that large parts of the MoVW mixed oxide precursor consist of about 10 μm large spherical segments (Fig. 4). A higher resolved image (not shown) did not reveal particle shapes, which would indicate crystalline material. SE imaging (Fig. 4B) and backscattered electron (BSE) imaging modes (Fig. 4A) of operation were used in combination with EDX analysis to investigate the elemental distribution of Mo, V, and W. The elemental compositions of two different spots in the BSE image were determined by EDX. While the W concentration was comparable (9 and 8 at.%), concentration variations were detected for Mo and V with 51 and 43 at.%, and 20 and 27 at.%, respectively. The regular shape of the detected EDX signals confirms that the observed elemental inhomogeneities are not due to an ill-defined sample-detector geometry. A comparison of the BSE and the SE image of the same particle fragment showed differently bright ar-

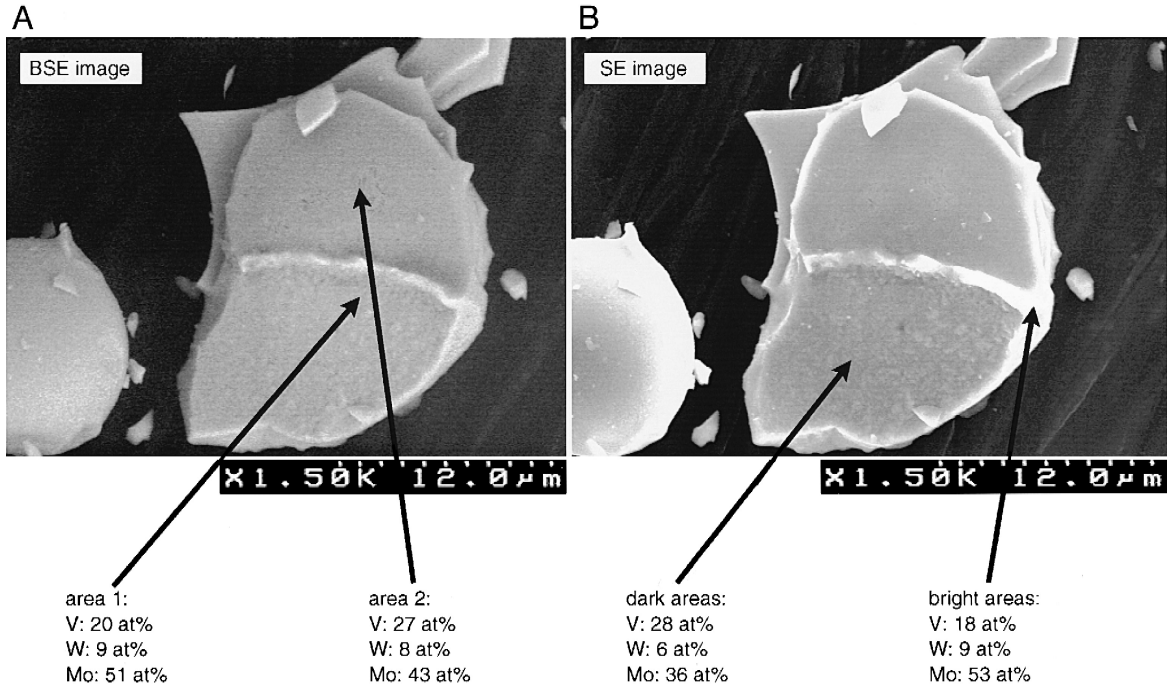

Fig. 4. (A) Backscattered secondary electron (BSE) SEM micrograph of untreated MoVW mixed oxide catalyst (the arrows indicate the spots at which EDX analysis was performed). (B) Secondary electron (SE) SEM micrograph of untreated MoVW mixed oxide catalyst (the arrows indicate the spots at which EDX analysis was performed).

eas. EDX analysis revealed two phases with differing Mo and V concentrations, while the W content was comparable with 6 and 9 at.%, respectively. The bright area in the SE image had a high concentration of 53 at.% Mo relative to 18 at.% V. Dark areas in the SE image had an Mo concentration of 36 at.% but a content of 28 at.% V. The dark areas are identified with the outer surface of the spherical-like particles, while the bright ones were due to cleavage faces.

EDX mapping was conducted of a 900 μm^2 area in order to confirm this result. Fig. 5A shows the SEM image and the Mo, V, and W distributions are depicted in Fig. 5B,C,D, respectively. While the Mo and W concentrations showed a similar distribution (Fig. 5B and D), regions of about 5 to 10 μm in size were identified which had a high vanadium concentration (Fig. 5C) but were depleted in Mo and W (Fig. 5B and D). EDX spectra were recorded of a V rich and V depleted area (marked by arrows in Fig. 5C). Mo, V, and W concentrations of 59, 33, and 8 at.%, respectively, were determined for the V-rich area, while Mo, V, and W concentrations of 86, 5, and 8 at.%, respectively, were detected for V depleted areas.

TEM combined with EDX was used to further characterize particle morphology, the elemental distribution and the presence of nanocrystalline material in the mixed precursor oxide. TEM images (Fig. 5E) revealed that the primary particles were smaller than 100 nm and did not exhibit regular shapes. The primary particles formed larger agglomerates of submicron size (Fig. 5E). Unlike the SEM–EDX result, spatial differences in the Mo, V, and W concentrations could not be detected for submicron sized agglomerates or the smaller primary particles (Fig. 5F,G,H). More details about the high resolution TEM and electron diffraction characterization will be described in a subsequent publication [65].

The SEM images of the thermally activated catalyst (Fig. 6A) show spherical particles. In contrast to the untreated MoVW oxide, these particles were

agglomerates of platelet-like crystallites of a few hundreds of nanometers in size (Fig. 6B). However, there remained parts of the sample which still showed irregular particle shapes (not shown). EDX characterization of 1 to 3 μm sized platelet-like crystals (Fig. 6C) revealed almost the exclusive presence of Mo with 32 at.% and only small concentrations of V (3 at.%), and W (1 at.%). Particles with an irregular habit (Fig. 6D) had higher concentration of V (19 at.%) and W (3 at.%) relative to Mo (30 at.%).

SEM–EDX mapping of a 900 μm^2 large area was used to probe the elemental heterogeneity after thermal activation (Fig. 7A). While the Mo (Fig. 7B) and W concentration distributions (Fig. 7D) were similar throughout the analyzed sample (Mo 71 at.%, V 11 at.%, W 18 at.%), an area of about 5 to 10 μm size was detected which shows a high V (Fig. 7C) concentration (44 at.%) and reduced Mo (48 at.%) and W (8 at.%) contents. Thermal activation did not lead to homogeneous element distribution on this length scale.

TEM–EDX determined the element distribution of the thermally activated catalyst on the submicron scale (Fig. 7E,F,G). In contrast to the untreated mixed oxide, the thermally activated catalyst exhibited an inhomogeneous element distribution. Thermal activation led to segregation of V on the submicron regime.

In summary, SEM, TEM, and EDX techniques show that the mixed oxide precursor is characterized by an inhomogeneous elemental distribution on the length scale of a few microns. The element distribution is homogeneous on the submicron scale. The particle shapes do not point to the presence of well-crystallized materials. The results may be explained by the preparation procedure. Different solubilities of the ammonium precursors most probably led to elemental inhomogeneities during the drying process. Thermal activation led to the formation of regular particle shapes pointing to crystallization and to vanadium segregation on the submicron scale.

3.3.2. RBS: bulk stoichiometry

The RBS spectra of the untreated mixed oxide, the thermally activated catalyst, and the corresponding simulations are displayed in Fig. 8 and the quantification is summarized in Table 2. The RBS metal concentrations confirm the values obtained by RFA and global SEM–EDX, both techniques exhibiting a larger error margin of approximately 10%. RBS determined concentrations of 16% Mo, 7.5% V, 2.1% W and 74.4% O for the untreated mixed oxide and of 16.5% Mo, 7.3% V, 2.2% W and 74.0% O for the thermally activated catalyst. These concentrations give total metal stoichiometries of $Mo_{0.636}V_{0.282}W_{0.082}$ for the untreated, and of $Mo_{0.641}V_{0.275}W_{0.083}$ for the thermally activated catalyst. A comparison with the formal stoichiometry of $Mo_{0.68}V_{0.23}W_{0.09}$ due to preparation evidences that the mixed oxide catalyst contains about 4% less Mo and 1% less W, but about 5% more V. This difference in the metal stoichiometry may be explained by weighing errors due to the uncontrolled water content of the starting ammonium polyoxo metallates. TG confirmed a water and ammonia content of the precursor oxide of minimum 2 wt.% when referenced to MoO_3 (Fig. 2). When referenced to the RBS stoichiometry of $MO_{2.9}$ (vide supra), the starting material contained 5% water and ammonia.

The bulk concentrations of the different metal ions change upon thermal activation. Thus, the (MoW) to V concentration ratios slightly increased from 2.5 to 2.6 upon activation. This points to a preferential loss of only about 3% of the total amount of 28% V. Vanadium oxide has its melting point at 963 K and hence, a vapor pressure at 823 K. Changing metal concentration ratios were also detected for the catalyst surface region by XPS (see Section 3.3). The RBS bulk metal to V concentration ratio for the untreated catalyst is two times higher than the XPS surface metal to V concentration ratio. For the activated catalyst, the bulk metal to V concentration ratio is about three times higher than this surface ratio. These observations can be explained by V-depleted surface-near regions relative to the bulk oxide. Due to the integral detection mode of the RBS technique and in contrast to the surface sensitive XPS result of a changing V concentration, the RBS finding cannot be explained as the XPS result by segregation of a V-containing phase which was also determined by EDX. Therefore, it is suggested two process change the metal concentrations. The main process is vanadium segregation and phase separation (XPS, EDX), and the minor one is loss of V by evaporation.

The total oxygen concentration of the untreated mixed oxide as determined by RBS decreased from about 74.4% O to 74.0% O for the thermally activated catalyst. From these values, an integral stoichiometry of $MO_{2.90}$ can be calculated for the untreated, and of $MO_{2.84}$ for the thermally activated mixed oxide. The latter RBS oxygen stoichiometry can be compared with the TG result (Fig. 2) and the XRD detection of Mo_5O_{14} ($MoO_{2.8}$) (Fig. 14). These results reveal that the actual catalyst is in fact a mixture of phases because Mo_8O_{23} and Mo_5O_{14} are the only crystallographically defined oxides in this stoichiometry regime, the latter being clearly ruled out by the structural analysis.

3.3.3. Photoelectron (XPS and UPS) and ion scattering spectroscopy (ISS): surface composition

In Table 3, the spectral parameters are compared with the Mo $3d_{5/2}$ XP spectra of the untreated mixed oxide, thermally activated catalysts, and the used catalysts (Fig. 9). Mo^{6+} and Mo^{5+} species present in the samples led to one unresolved peak at 233.6 eV due to spatial inhomogeneities of the electric structure causing preferential charging which is the consequence of the elemental heterogeneity as detected by SEM–EDX and TEM–EDX. Mo^{4+} species were detected in separate signals at 230.4 eV probably due to the higher conductivity of these higher reduced parts of the specimens [66,67].

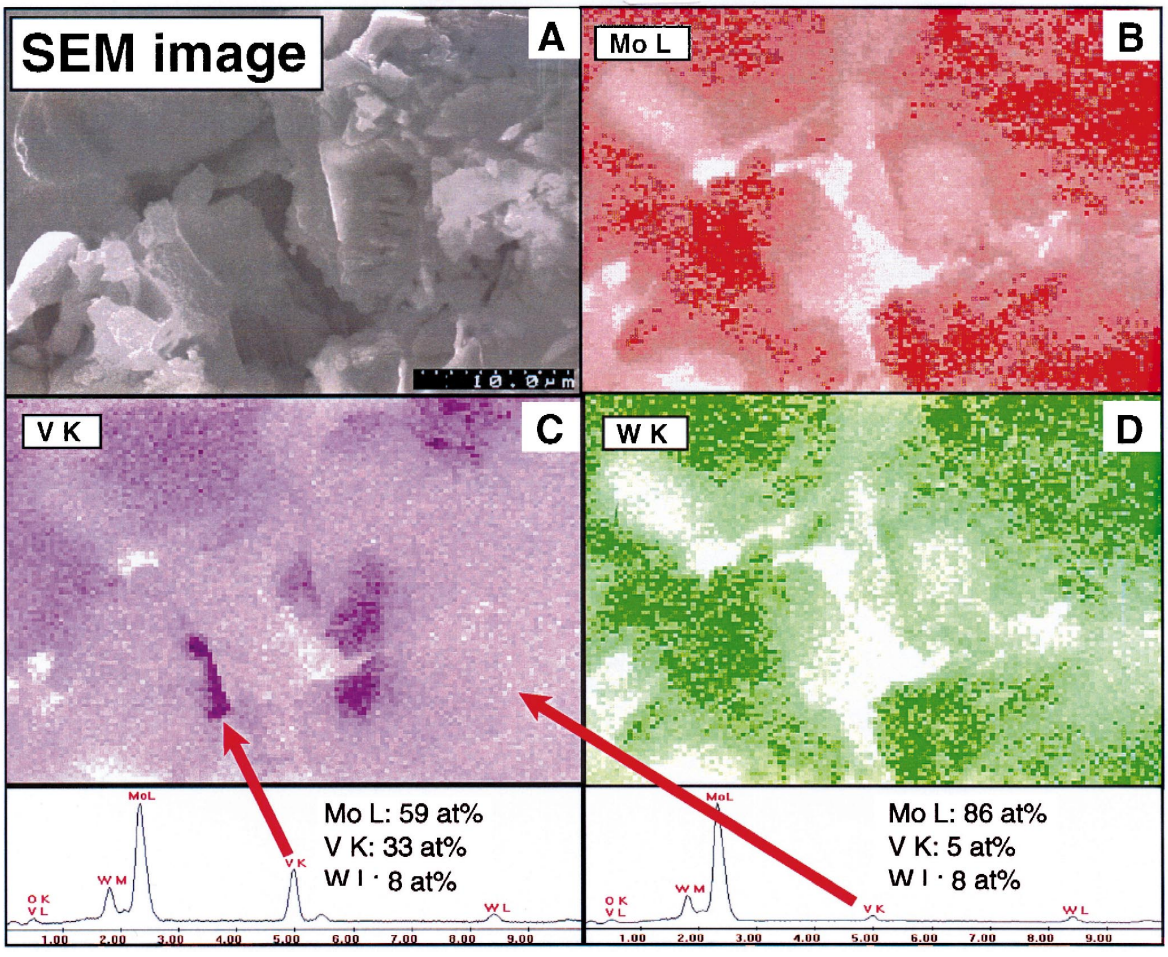

Fig. 5. SEM–EDX mapping of an area of 900 μm^2 of untreated MoVW mixed oxide: (A) SEM image; (B) Mo-, (C) V-, and (D) W-EDX mapping. TEM–EDX mapping of untreated MoVW mixed oxide: (E) TEM image; (F) Mo-, (G) V-, and (H) W-EDX mapping.

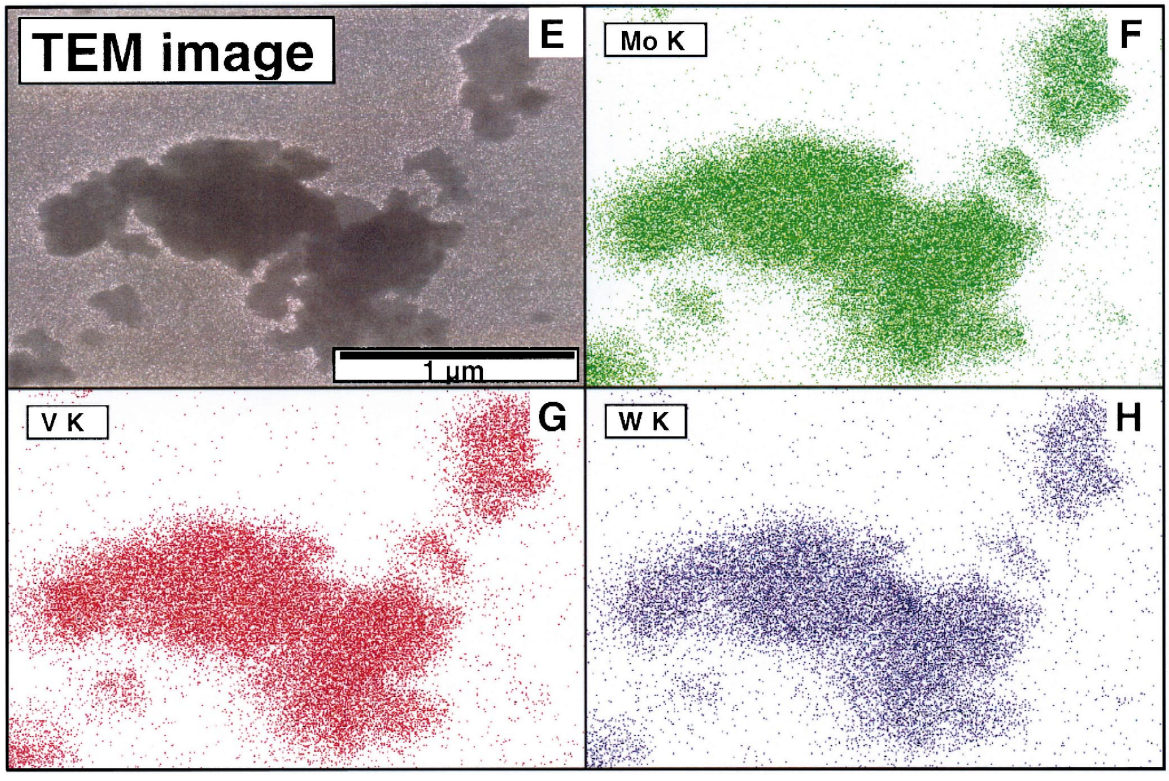

Fig. 5 (*continued*).

Curve fitting was conducted in order to determine the contributions of Mo^{6+}/Mo^{5+} and Mo^{4+} ions, the XPS signals. The spin–orbit splitting between the Mo $3d_{5/2}$ and $3d_{3/2}$ signals was fixed to 3.1 eV, the intensity ratio of the Mo $3d_{5/2}$ and $3d_{3/2}$ signals was set to 0.66 (theoretical value: 0.6), as determined for the MoO_3 reference (Table 3). Deconvolution of the Mo^{6+} and Mo^{5+} was not attempted due to spatial differential charging. The signal positions were fixed, signal intensities and half widths were varied to give optimum fit.

The Mo 3d BEs reported in the literature increased in values during recent years. This fact points either to charging problems or to a partial reduction of MoO_3 under XPS conditions (vide infra). In a recent publication, Aigler et al. [66] determined the Mo^{6+} $Mo3d_{5/2}$ BE to be 233.2 eV with an FWHM of 2.6 eV, the one of Mo^{5+} to be 232.1 eV with FWHM of 2.5 eV, and the BE of Mo^{4+} with 230.2 eV with an FWHM of 2.3 eV.

Unfortunately, the catalyst which was thermally activated in the reactor had to be exposed to air for transfer to the XPS chamber. This transfer may lead to uncontrolled reoxidation or sample contamination. Therefore, the untreated mixed oxide was additionally activated in a reaction cell attached to the XPS chamber at 813 K for 2 h. The sample can be directly transferred from this reaction cell to the XPS chamber without exposure to air. This thermal activation also led to the development of a new peak at 229.6 eV (Fig. 9, Table 3). By comparison with data reported by Grünert et al. [67], the observed signals at 232.8 and 229.5 eV are assigned to unresolved $Mo^{6+/5+}$ and Mo^{+4} oxidation states with the relative concentrations of 87% and 14%.

The deconvolution of the XP spectrum after activation in the reactor and transfer to the XPS reveals changes comparable to those after the thermal activation in the XPS reaction cell, however, less pronounced. The concentrations of $Mo^{6+/5+}$ and Mo^{4+}

were determined to be 95% and 5%, respectively. This may be accounted for by the unavoidable exposure to air. Therefore, it may be assumed that thermal activation in the reactor leads to a reduction of the catalyst surface comparable to that after the treatment in the XPS reaction cell. In addition, the total surface concentration of Mo has increased by the thermal activation, while the V and W content had decreased.

The XPS characterization after catalysis under increased oxygen partial pressures (Table 3 and Fig. 9) revealed concentrations of $Mo^{6+/5+}$ and Mo^{4+} of

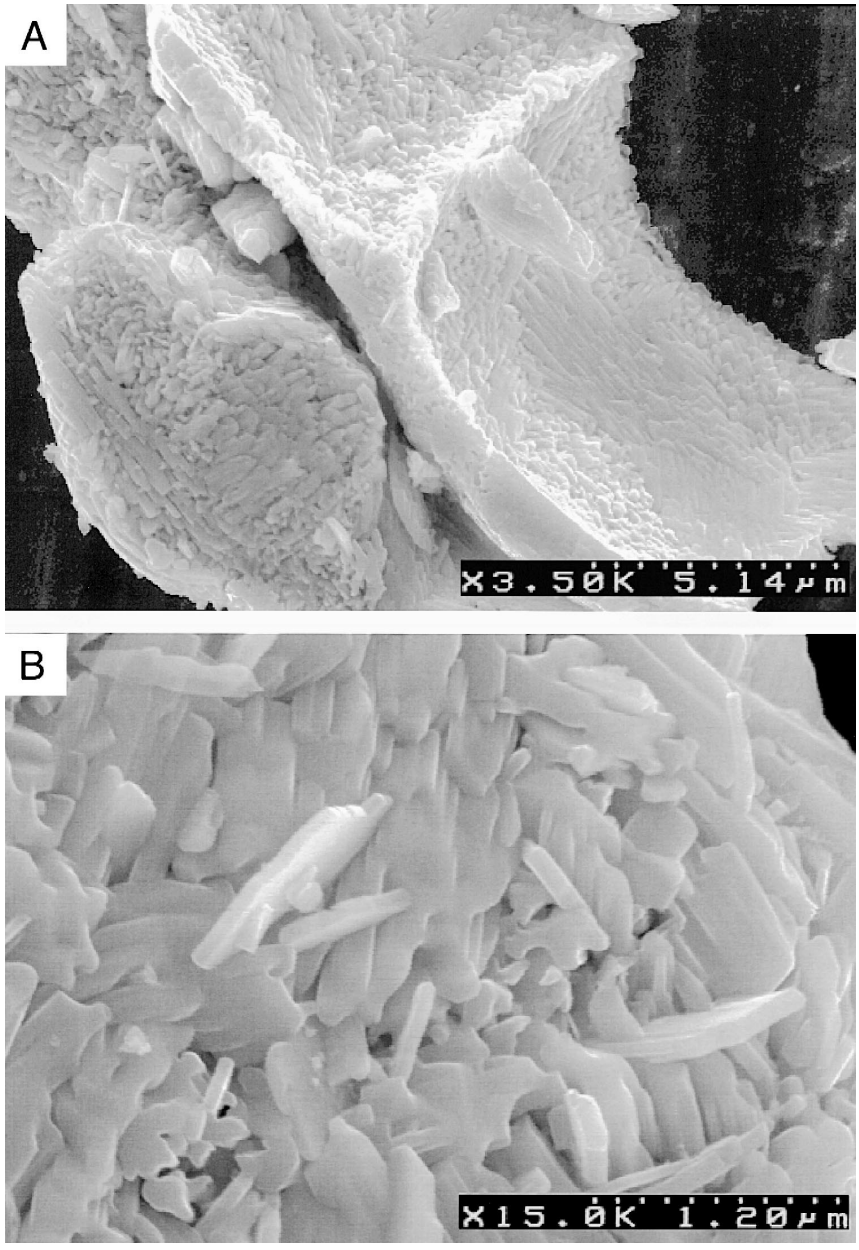

Fig. 6. (A,B,C,D) SEM images of the thermally activated mixed oxide catalyst. Arrows indicate the spots of the EDX analysis.

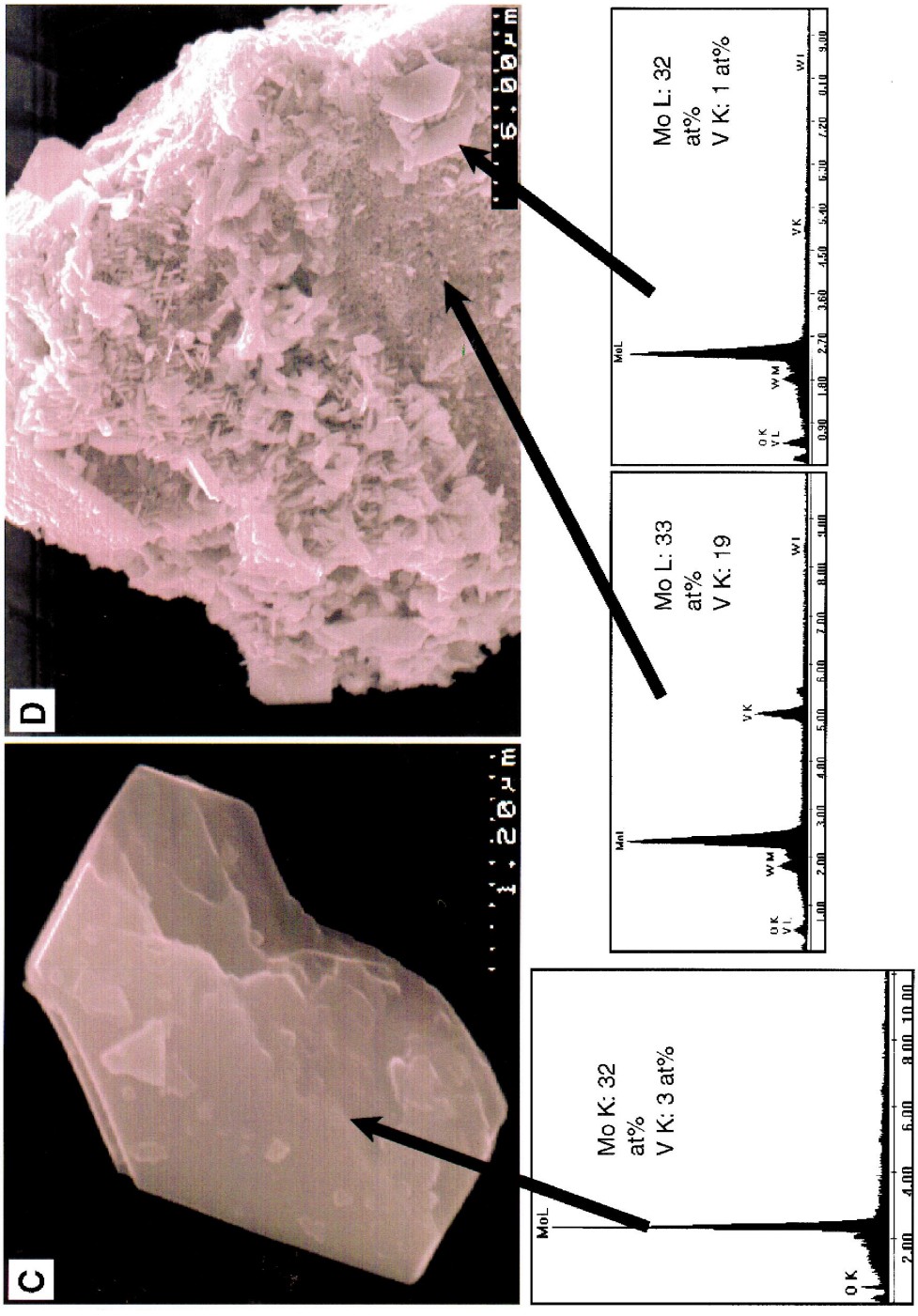

Fig. 6 (*continued*).

96% and 4%. It is evident that the concentration of Mo^{4+} had decreased relative to that of $Mo^{6+/5+}$ as compared to the activated catalyst. If one assumes that in situ thermal activation in the reactor prior to catalysis had led to a degree of reduction comparable to that after activation in the XPS reaction cell, the relative changes in the concentrations of $Mo^{6+/5+}$ and Mo^{4+} were initially even more pronounced.

The V $2p_{3/2}$ XP spectra and their parameters are displayed in Fig. 10 and in Table 3 of the untreated mixed oxide, the oxide activated in the XPS cell, and in situ in the reactor, and of the used catalyst and compared with the V_2O_5 reference. The signal positions were kept constant for the V^{5+} and V^{4+} contributions, the integrated signal intensities and FWHM were varied to fit the spectra. The variations in the line widths can easily be accounted for by the sample inhomogeneities and therefore preferential, differential charging.

The V 2p XP signal (Fig. 10) of the untreated mixed oxide consists of two components at 517.2 and 516.4 eV (Table 3). The component at higher binding energy can be assigned to V^{5+} by comparison to V_2O_5 (Table 3) and the reported value of 517.5 eV for V^{5+} [68]. The component at lower binding energy corresponds to V^{4+} by comparison with the literature value of 516.3 eV [68]. Similar to the Mo 3d spectra, V undergoes reduction during the

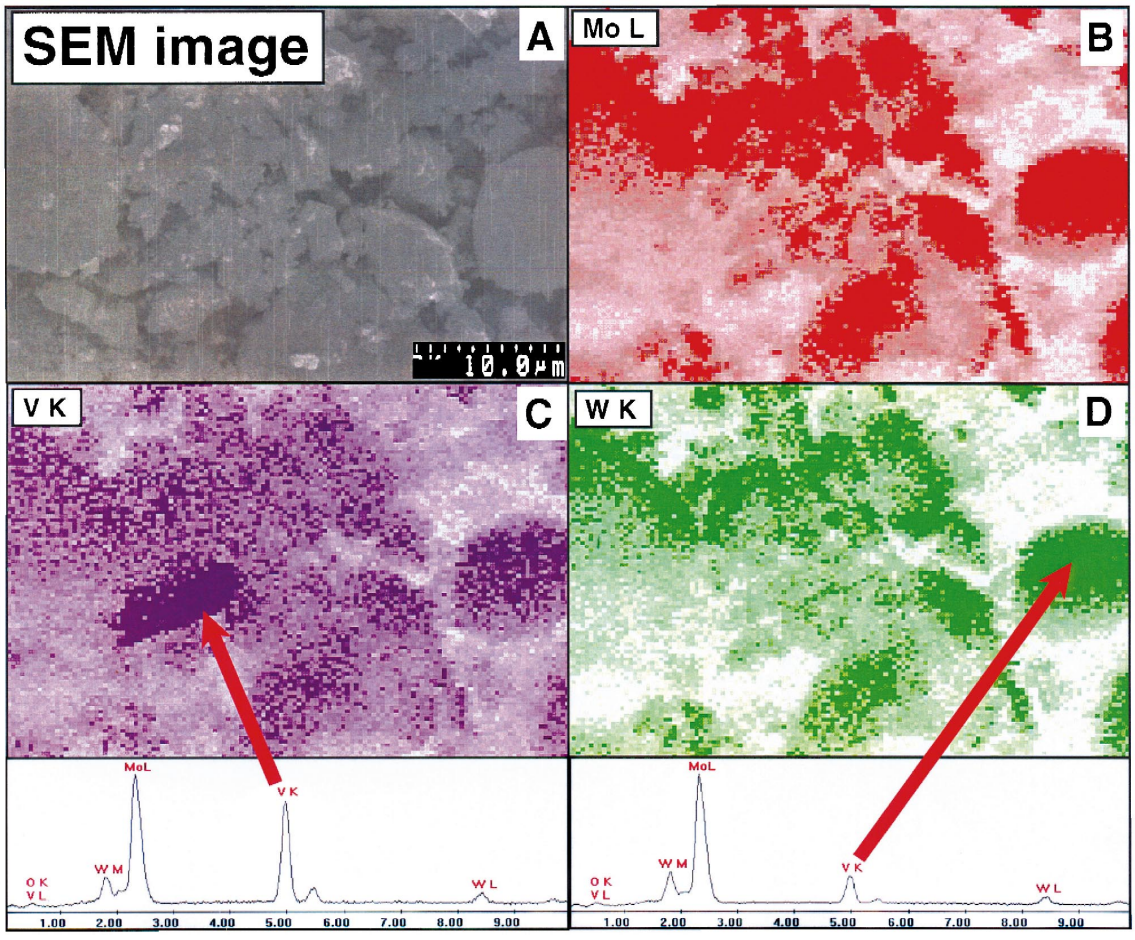

Fig. 7. SEM–EDX mapping of an area of 900 μm^2 of thermally activated mixed oxide: (A) SEM image; (B) Mo-, (C) V-, and (D) W-EDX mapping. Arrows indicate the spots at which the EDX spectra were recorded. TEM–EDX mapping of thermally activated mixed oxide:(E) Mo-, (F) W-, and (G) V-EDX mapping.

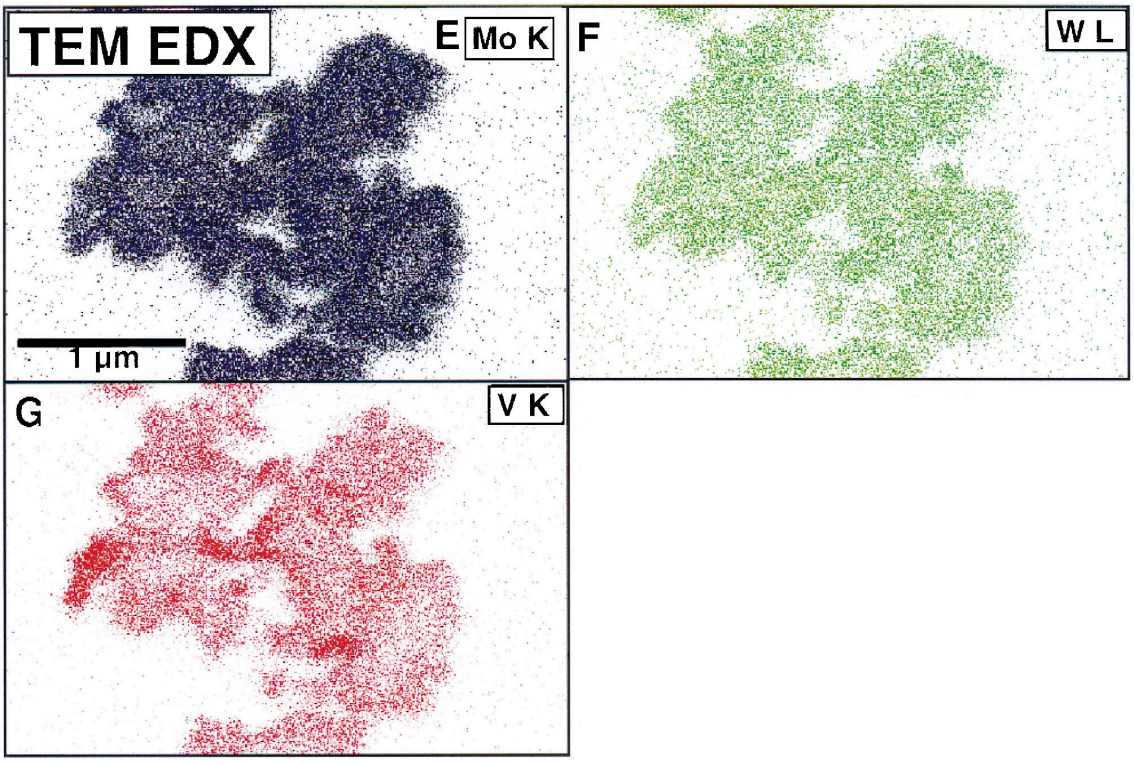

Fig. 7 (*continued*).

thermal activation (Table 3). Thermal activation in the XPS reaction cell led to a reduction of the V^{5+} contribution from 64% to 45%, whereas the concentration of V^{4+} increased from 46% to 55%. These values are comparable to the V^{5+} and V^{4+} content after thermal activation in the reactor and transfer to the XPS chamber, which gave 47% and 53%, respectively. Thus, transfer to the XPS chamber did not result in a V^{4+} reoxidation comparable to that observed for Mo^{4+}. SEM– and TEM–EDX analysis observed the segregation of V. In addition, XPS quantification of the V surface concentration after thermal activation revealed a decrease in the V content by 12%, confirmed by ISS showing a decrease by 17%. Therefore, the astonishing result of a stable V^{4+} state may be explained by this V segregation into the subsurface layers with no access of gaseous oxygen.

XPS analysis after catalysis under high oxygen partial pressures (Table 3) reveals a further reduction of the V^{5+} concentration to 43% and, thus, an increase in the amount of V^{4+} to 57%. The V^{4+} states are not reoxidized after catalysis under high O_2 pressures (Table 3) comparable to Mo^{4+}. The stability of V^{4+} centers toward reoxidation can again be understood when considering the quantitative changes in the surface concentrations (Table 3). The surface V concentration had decreased by segregation into the bulk and phase separation as shown by EDX. Thus, the formation of VO_2, whose presence in the sample was not ruled out by RXD, could explain this observation of stable V^{4+} due to its high stability. Moreover, reoxidation of bulk V is inhibited relative to that of surface V. The presence of a high concentration of V^{4+} centers in the bulk oxide may indeed point to their role in catalysis. V^{4+} may optimize the electron transport properties of the active oxide catalyst.

In Table 3, the spectral parameters are listed of the W $4d_{5/2}$ XP spectra (Fig. 11) of the untreated mixed oxide, the thermally activated catalysts, and used catalysts are compared with the WO_3 reference.

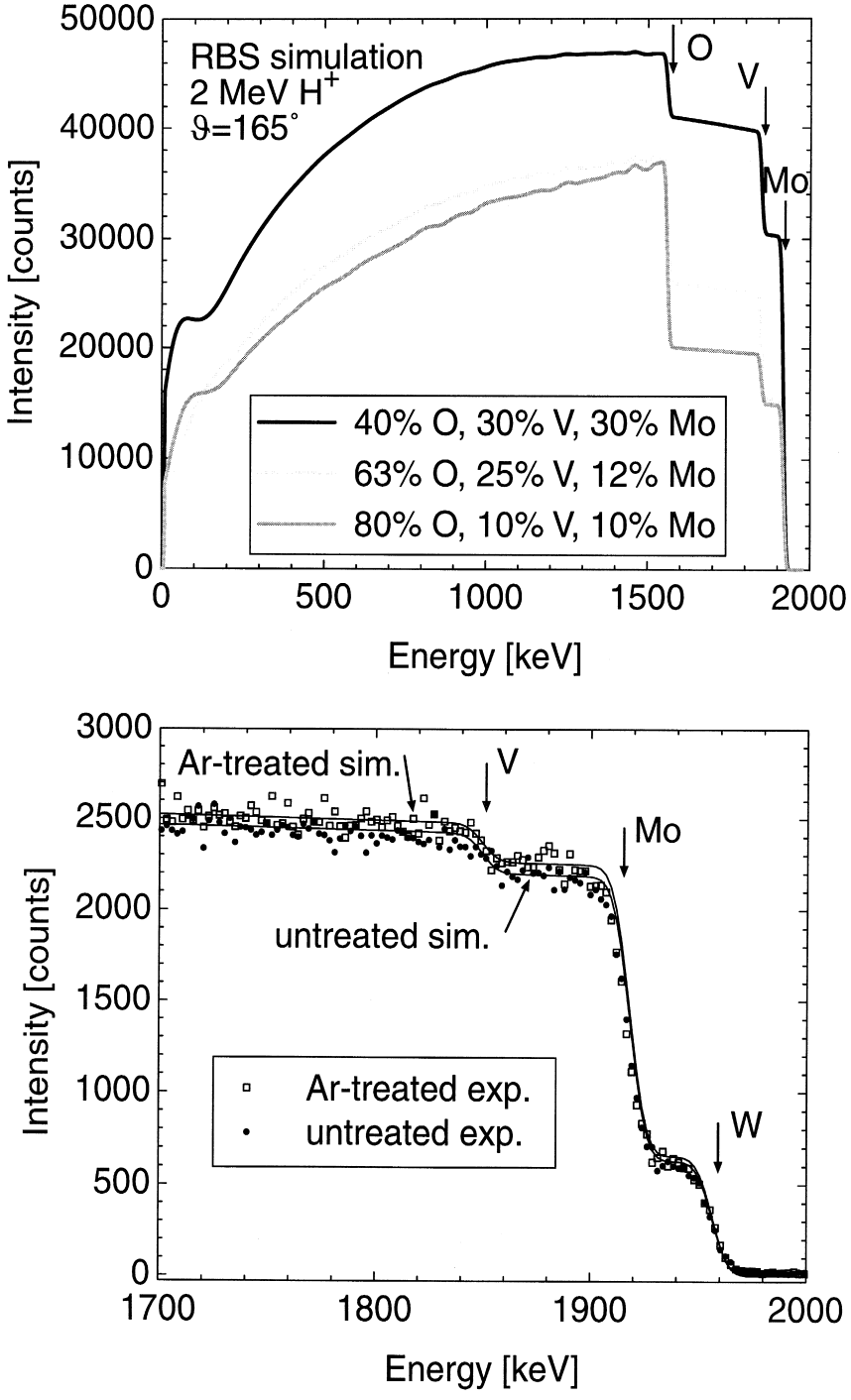

Fig. 8. RBS simulation (above) to determine optimum experimental conditions. Measured (dots) and calculated (solid line) RBS spectra (below) of the untreated mixed oxide and the thermally activated catalyst.

Table 2
Element concentrations of the pristine catalyst and the activated mixed oxide catalyst in at.%

Sample	O	Mo	V	W	ΣM/V
Formal stoichiometry	–	68	23	9	3.4
RBS					
Untreated oxide	74.4	16	7.5	2.1	
	–	63.6[a]	28.2[a]	8.2[a]	2.5
Activated catalyst	74.0	16.5	7.3	2.2	
	–	64.1[a]	27.5[a]	8.3[a]	2.6
RFA[b]					
Untreated oxide	–	69.5	20.7	8.7	
Global SEM – EDX[b]					
Untreated oxide	–	64.7	24	11.3	
Activated catalyst	–	79	13	8	
Potentiometric NH_4^+ analysis					
Untreated oxide	14 mol%				
Activated catalyst	0				

[a] Normalized to sum of metals 100% for comparison with RFA and SEM–EDX analysis.
[b] Normalized to sum of metals 100% due to uncertainty in oxygen determination.

Only the FWHM had to be varied in order to fit the experimental spectrum. The changing FHWM can be accounted for by differential charging due to sample inhomogeneities as detected by EDX. A W^{5+} contribution at the low energy wing of the W $4d_{5/2}$ was not observed. In contrast to Mo 3d and V $2p_{3/2}$, W is not reduced. Hence, W may serve as a structural promotor as frequently stated in the literature.

XPS on MoO_3, MoO_2 and intermediate crystalline oxide references revealed Mo:O ratios strongly deviating from the theoretical values [69]. Thus, an Mo:O ratio of 2.45 was observed for well- crystallized MoO_3, 2.8 for Mo_8O_{23}, and 2.3 for MoO_2. This deviation from the theoretical values are most probably due to the UHV conditions under which MoO_3, which is nonstoichiometric even at normal conditions [70], loses oxygen. MoO_2, on the other hand, is reoxidized at its surface when stored in air. These too low oxygen concentrations for MoO_3 and the too high one for MoO_2 has to be considered when comparing XPS and RBS results. The thermal activation reduces the total metal to oxygen ratio from 2.4 for the untreated to 2.3 for both thermally activated catalysts (Table 3). Hence, the degree of reduction of the MoVW mixed oxide cannot be deduced precisely enough from the overall M:O ratio.

ISS, sensitive to the outermost atomic layer, was used to obtain data on a changing surface metal composition complementary to the XPS results. The disadvantage of powder ISS, however, is the impossibility of quantification due to unknown shadowing effects in the specimen. Fig. 12 shows the ISS spectra of the untreated mixed oxide (open circles) and the thermally activated catalyst (open squares). The outermost surface layer of the thermally activated catalyst is depleted in V and W, whereas the surface concentration of Mo has increased. The relative changes of the ISS signals in percent are given in Fig. 12. A higher bulk V concentration was proven by ISS depth profiling. An increase of the V and W signal intensities (open upward triangles) was observed after 10 ISS scans. This proves bulk segregation of vanadium and tungsten relative to Mo.

The He I (Fig. 13A) and He II spectra (Fig. 13B) of the untreated and the thermally activated catalyst confirm the partly reduced state of the surface by the development of a band close to the Fermi level with emission maxima at 1.6 eV (He I) and 1.4 eV (He II), respectively. The valence band emission arises from overlapping O and Mo orbitals as suggested by theoretical calculations on V_2O_5 [71] and MoO_3 [72]. The energetically high and low laying contributions to the valence band contain strong admixtures of metal d-states to the O 2p states, whereas the energetically intermediate region of the valence band arises from more oxygen atom-like O 2p emissions. The difference in the spectral shape of the He I and He II spectra are explained by the different cross-sections for the interactions of photons with the hybridized Mo4d, V3d, W5d and O2p states of the valence band. Thus, the cross-section of O 2p with He I is 10.67, with He II it is 5.18, that of V 3d with He I is 5.81, with He II it is 5.94, and that of Mo 4d with He I is 26.27, and with He II it is 8.49. Hence, He I excitation is more sensitive to upper valence band states, while He II probes lower laying contributions. This difference in cross-sections is reflected in the more pronounced intensity changes of the He I spectrum of the Mo4d defect states at 1.6 eV and of the He II spectrum of the metal states above 10 eV

Table 3
Mo 3d XP spectral parameters of the differently treated mixed oxides

Binding energy [eV]		$Mo^{6+/5+}$ $3d_{5/2}$	Mo^{4+} $3d_{5/2}$	V^{5+} $3d_{5/2}$	V^{4+} $3d_{5/2}$	W^{6+} $4d_{5/2}$	O1s (531, 5 eV)/ ΣM[a]	ΣM/V
		233.6	230.4	517.8	516.5	248.7		
Untreated	Intensity [%]	99	1	63.5	36.5		2.4	5.3
oxide	FWHM [eV]	1.7	–	1.8	1.8	5.6		
	Σ metal	67[b]		16[b]		17[b]		
N_2 activation	Intensity [%]	86	14	44.8	55.2		2.3	6.1
(ESCA cell)	FWHM [eV]	2.4	1.1	1.8	1.8	6.4		
	Σ metal	70[b]		14[b]		16[b]		
Ar activated	Intensity [%]	95	5	47	53		2.3	10.0
catalyst	FWHM [eV]	2	2	1.9	1.9	5.5		
	Σ metal	74		9[b]		16[b]		
Ar activated	Intensity [%]	96	4	42.6	57.4		–[c]	4.3
catalyst after	FWHM [eV]	2.5	2.5	2.1	2.1	6.6		
catalysis	Σ metal	56		19[b]		25[b]		

Compound	Position [eV]		Intensity ratio	FWHM	Gaussian %
MoO_3	Mo $3d_{5/2}$: 233.7	Mo $3d_{3/2}$: +3.1	$3d_{5/2}/3d_{3/2}$: 0.66	1.68	0.26
V_2O_5	V $2p_{1/2}$: 517.1		–	1.31	0.26
WO_3	W $4d_{5/2}$: 248.2		–	4.3	0.26

[a] ΣM = sum of all metals.
[b] at.%, Normalized to sum of metals 100%.
[c] Not determined because of incompletely removed quartz wool.

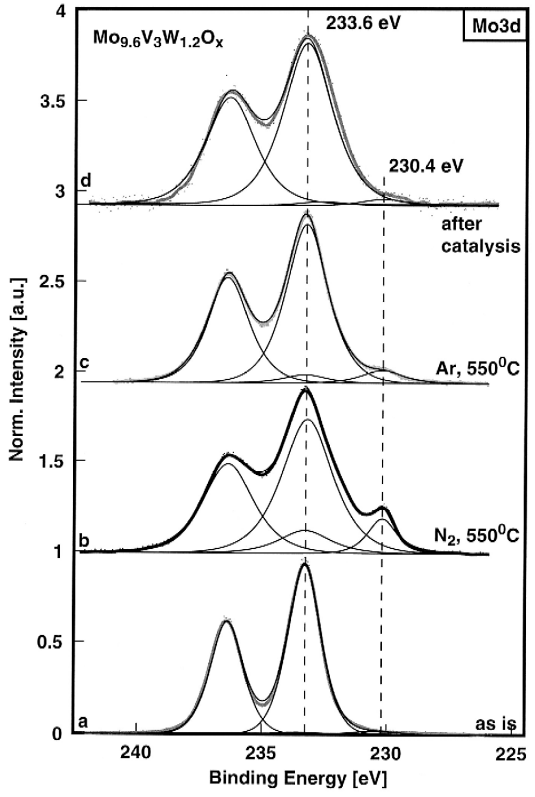

Fig. 9. Deconvolution of the Mo(3d) XP spectra of (a) the untreated mixed, (b) the Ar activated, and (c) N_2 activated catalyst, and (d) the catalyst after reaction under high oxygen partial pressures.

upon thermal activation. Hence, the changed spectral shapes reflect changes in the local chemical bonding of surface-near oxide layers. This observation is related to the XRD and Raman indications of crystallization. Although, it must be pointed out that the surface-near regions of the oxide most probably exhibit a geometric structure different from the bulk. The UPS observation of a new defect-induced conduction band close to the Fermi level indicate the occurrence of electronic conduction due to delocalized, defect-induced bands. Such a semi-metallic (absence of a Fermi edge) surface structure is essential for the reductive activation of oxygen. The XPS/ISS results discussed above imply this conduction band is composed of Mo–O species, the surface is depleted in vanadium after thermal activation.

3.3.4. XRD of the MoVW mixed oxide

This type of MoVW mixed oxide material was already investigated by Werner et al. [43] who used XRD and HRTEM for structural characterization. The XRD pattern of the present mixed oxide precursor is shown in Fig. 14 together with simulated XRD patterns of nanocrystalline Mo_5O_{14} and MoO_3. The experimentally determined cell parameters as well as the simulation parameters are given in Table 4. The experimental XRD pattern fully confirms the results reported by Werner et al. [43]. The MoVW mixed oxide was found almost XRD amorphous (Fig. 14) and the XRD pattern was interpreted as being composed of nanocrystalline Mo_5O_{14}-like and MoO_3-like oxides. The two very broad reflections at about 23° and 27° 2θ may be attributed, according to the simulated diffraction patterns, to the main metal–

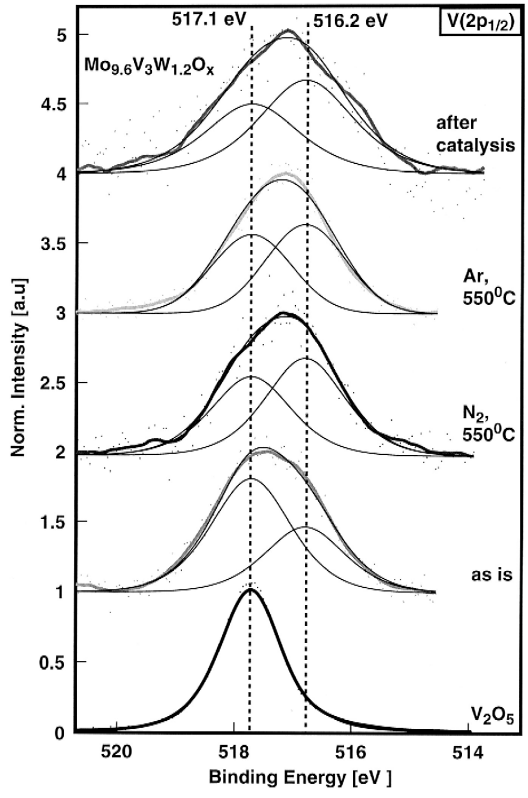

Fig. 10. Deconvolution of the V(2p) XP spectra of the (a) untreated, (b) the Ar activated, and (c) N_2 activated catalyst, and (d) the catalyst after reaction under high oxygen partial pressures.

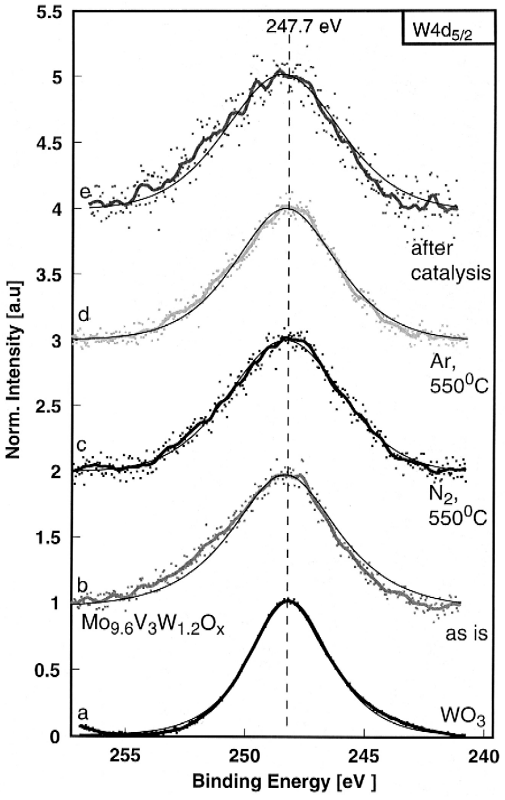

Fig. 11. Deconvolution of the W(4d) XP spectra of the (a) untreated, (b) the Ar activated, and (c) N_2 activated catalyst, and (d) the catalyst after reaction under high oxygen partial pressures.

metal distances of ~4 Å found in Mo_5O_{14}-type oxides and of ~3 Å found in MoO_3-like oxides, respectively. According to the XRD simulations, the presence of nanocrystalline V_2O_5 has to be excluded for the untreated mixed oxide. The X-ray coherence lengths between 100 and 1500 pm, which were used for the simulation of the Mo_5O_{14} and MoO_3 patterns, compare well with the TEM observation of particles smaller than 100 nm.

The XRD pattern of the thermally activated mixed oxide is also presented in Fig. 14 together with its simulation. The experimentally observed cell parameters and the simulation parameters are also given in Table 4. The crystallinity has increased after thermal activation, in agreement with Werner et al. [43] who also observed crystallization at 773 K in air. Two phases were positively identified by XRD in the present samples. The main MoVW phase is represented by a structure similar to that of Mo_5O_{14}. The minority MoVW phase was identified in trace amounts as being similar to MoO_3. In addition, the presence of traces of MoO_2 and VO_2 cannot be excluded from the experimental diffractogram. This result was confirmed by a calculation of the theoretical XRD pattern of Mo_5O_{14} and MoO_3. The increased crystallinity of Mo_5O_{14} is also reflected in the coherence length parameters of the simulated pattern, which are about 30 nm. The incorporation of V or W in both these MoVW phases at Mo positions is not directly reflected by new reflections. Table 4 summarizes the calculated and experimental cell constants. The contraction of the *a*-axis and slight expansion of the *c*-axis of the $(MoVW)_5O_{14}$ unit cell as compared to Mo_5O_{14} indicates the incorporation of V and W into the real structure of this phase. Comparable expansions and contractions of the unit cell parameters were also observed for the real structure of the minority $(MoVW)O_3$ phase, also indicating the incorporation of V and W.

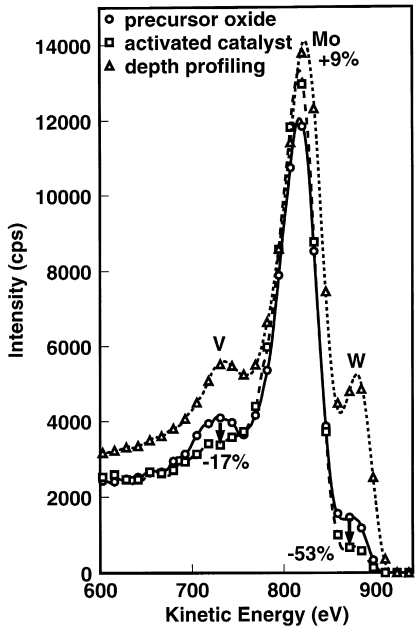

Fig. 12. ISS spectra of the untreated mixed oxide (open circles), the thermally activated catalyst (open squares), and of this material after depth profiling with 10 ISS scans (open upward triangles).

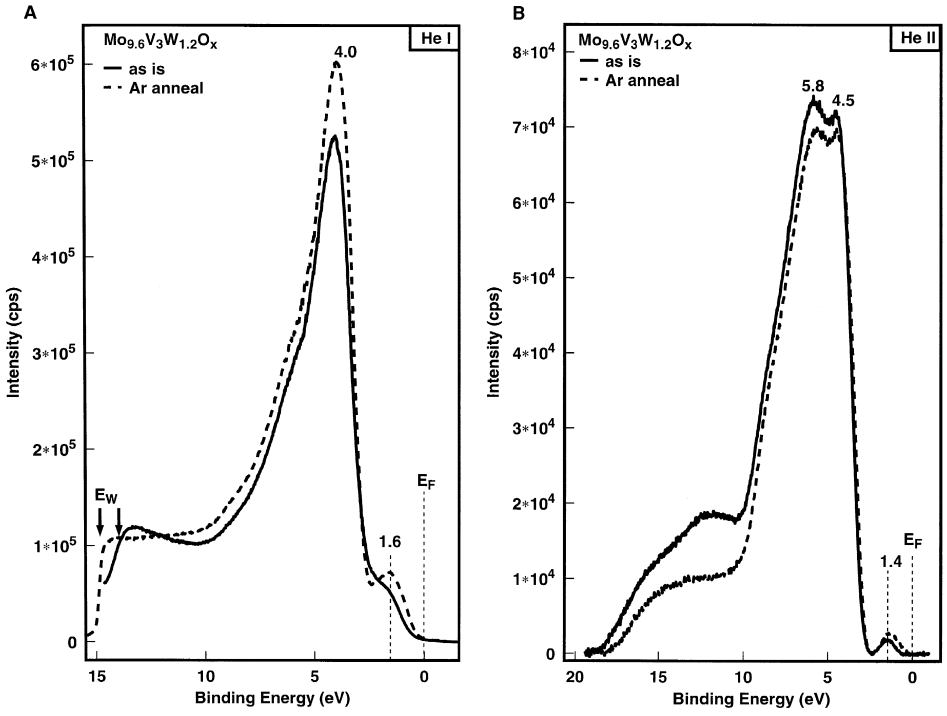

Fig. 13. (A) He I UPS spectra of the untreated mixed oxide (solid line) and the thermally activated catalyst (dashed line). (B) He II UPS spectra of the untreated mixed oxide (solid line) and the thermally activated catalyst (dashed line).

3.3.5. Confocal Raman microspectroscopy

Raman spectroscopy is suited to characterize the structure of X-ray amorphous materials. The special capabilities of laterally resolved confocal Raman microspectroscopy are combined with the SEM–EDX and XRD results. Raman mapping was done with the lowest possible laser power to avoid irradiation damage.

The Raman spectra of the untreated precursor oxide (Fig. 1a,b) showed only a broad ill-defined signal between 600 and 1000 cm^{-1} and a broad background in the lattice mode regime. The broad feature between 600 and 1000 cm^{-1} exhibits some structure at about 720(sh), between 830 and 860 cm^{-1}, and at 930 cm^{-1} These bands and shoulders occur in the typical regime of Mo−O vibrations. This observation confirms the XRD result of a nanocrystalline material. SIMPLISMA evaluation (data not shown) gave some additional information on the number of structurally different mixed oxide precursor species. The set of spectra can be calculated by linear combinations of two weighed spectral components. The spectral component 1 shows two features at about 930 and 870 cm^{-1}, while the spectrally pure component 2 shows a weak feature at about 900 cm^{-1} and a broad band centered at about 800 cm^{-1}. By comparison with the XRD result of Mo_5O_{14}- and MoO_3-like oxides in the precursor material, the spectral component 1 is attributed to the nanocrystalline Mo_5O_{14}-like, component 2 to the nanocrystalline MoO_3-like oxide.

Two Raman spectra (spectra a and b of Fig. 15A) recorded at different spots of the thermally activated catalyst confirm that the activated MoVW mixed oxide remained structurally inhomogeneous. Spectrum (a) of Fig. 15A shows bands at about 970(sh), 900, 850 and 710 cm^{-1}. Spectrum (b) exhibits bands at 740 and 580 cm^{-1}. The spectrally pure components of this set of 100 Raman spectra were determined by SIMPLISMA (spectra c, d, and e of Fig. 15A). The spectrally pure major component (spectrum c of Fig. 15A) exhibits bands or shoulders at

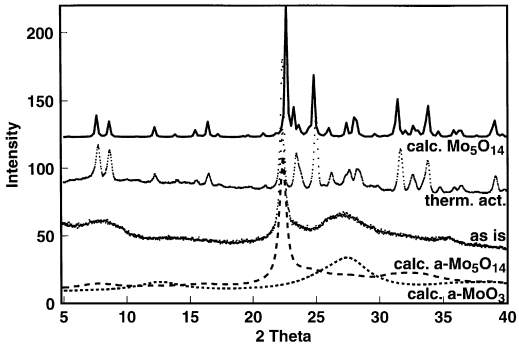

Fig. 14. XRD pattern of the untreated MoVW mixed oxide (dots) together with the simulations of nanocrystalline MoO_3 (short dashed line) and nanocrystalline Mo_5O_{14} (long dashed line); XRD pattern of the thermally activated MoVW mixed oxide (dots) and the simulated pattern of crystalline Mo_5O_{14} (solid line).

about 970, 900, 850 and 700 cm^{-1}. This component resembles the experimental Raman spectrum (a) of Fig. 15A. By comparison with the XRD result (Fig. 14), the major component of the Raman spectra is identified with the Mo_5O_{14}-type oxide present after thermal activation, and therefore may serve as a fingerprint for this oxide. All three transition metal ions, Mo, V, and W, however, have Raman bands due to M−O vibrations in this frequency regime depending on the coordination sphere and symmetry, and probably the degree of reduction. A detailed discussion of a possible assignment of the detected bands to definite metal–oxygen vibrations is given elsewhere [65]. Spectrum (d) of Fig. 15A represents one minority component of the thermally activated MoVW mixed oxide. It shows bands at about 740 and 580 cm^{-1} and is comparable to the experimental spectrum (b) of Fig. 15A. This component can be identified with MoO_2 by comparison with a reference spectrum of MoO_2 [69]. MoO_2 was also detected in trace amounts by XRD. The second spectrally pure minority component identified by SIMPLISMA (spectrum e of Fig. 15A) exhibits only very ill-defined, broad features with a broad maxi-

Table 4
Experimental unit cell parameters and literature data

Cell constants	Mo_5O_{14}		MoO_3	
	ICDD [pm]	Calculated [pm]	ICDD [pm]	Calculated [pm]
a	2299.5 (4599/2)	2273.2	396.2	395.4
b	2299.5 (4599/2)	2273.2	1385.8	1387.2
c	393.7	397.5	369.7	369.38

Simulation of experimental XRD patterns

Nanocrystalline Mo_5O_{14}[a,b]			Nanocrystalline MoO_3[a,b,c]	
Cell constants [pm]	Coherence length [pm]	Strain [%]	Coherence length [pm]	Strain [%]
$a = 2300$	2500	0	100	10
$b = 2300$	2500	0	250	0
$c = 397$	15 000	0	750	1

Crystalline Mo_5O_{14}[a,b]			Crystalline MoO_3[d]
Cell constants [pm]	Coherence length [pm]	Strain [%]	Crystalline MoO_2[d]
$a = 2285$	30 000	0	Crystalline VO_2[d]
$b = 2285$	30 000	0	
$c = 398.5$	40 000	0	

[a] Atom positions according to ICSD database.
[b] Simulation with pseudo-Voigt functions with 100% Lorentzian contribution.
[c] Preferential orientation of 25% along the 011 direction.
[d] Only trace amounts of oxides detected; number of experimental reflections too small for simulation.

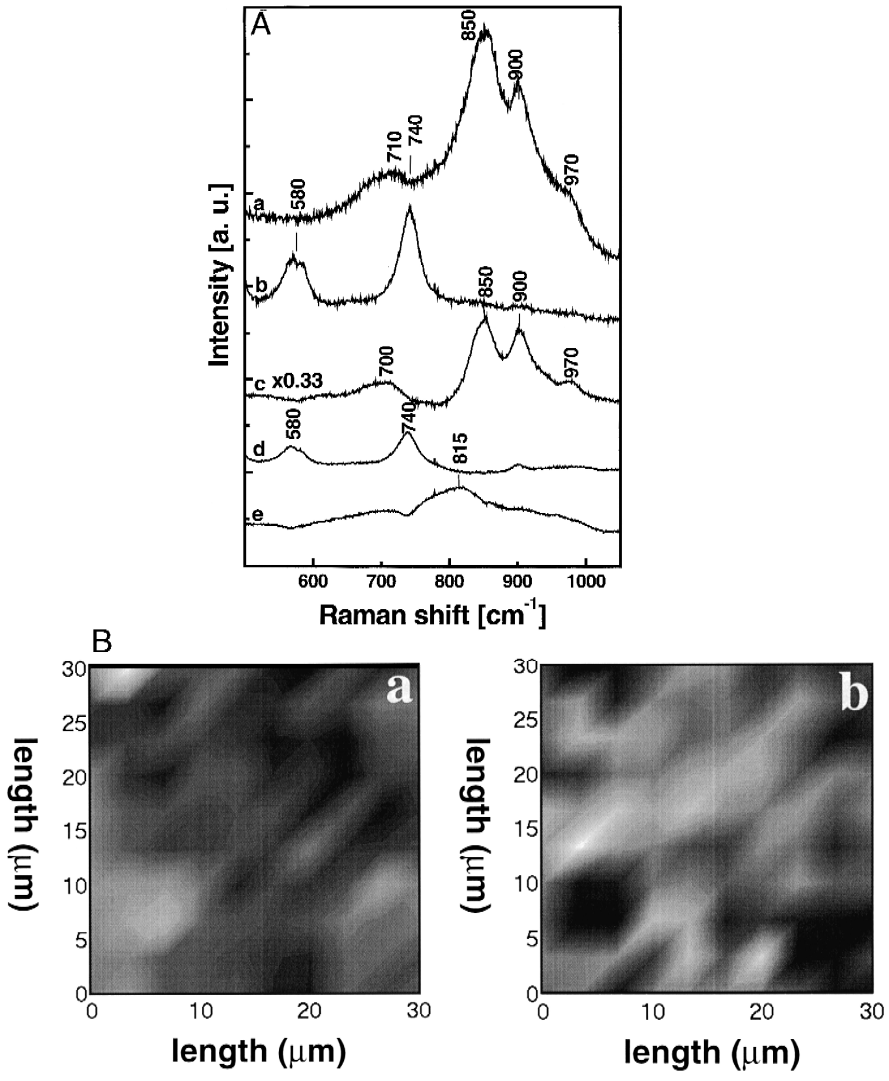

Fig. 15. (A) Two representative confocal Raman spectra (a, b) of thermally activated MoVW mixed oxide recorded at two different spots (lateral resolution 700 nm) with minimum laser power. Spectra c, d, and e: SIMPLISMA analysis of the set of 1000 laterally resolved confocal Raman spectra of thermally activated MoVW mixed oxide. Spectrum (c): spectrally pure majority component; spectrum (d): spectrally pure first minority component; and spectrum (e): spectrally pure second minority component. (B) Raman micro image (a) of the thermally activated MoVW mixed oxide as generated from the intensity of the Raman band at 740 cm^{-1} (first minority component) and 847 cm^{-1} Raman micro image (b) of the thermally activated MoVW mixed oxide as generated from the intensity of the Raman band at 850 cm^{-1} (majority component). Bright areas indicate strong band intensities, dark areas weak intensities.

mum at about 815 cm^{-1}. This component is identified with nanocrystalline MoO_3-type oxide. It is known that Mo_5O_{14} is metastable at its temperature of formation with respect to the disproportionation in MoO_3 and MoO_2 [16,44], which explains the detection of MoO_3- and MoO_2-type oxides.

In summary, Raman and XRD characterization of the thermally activated material reveal structural heterogeneity of the MoVW mixed oxide with Mo_5O_{14}-type oxides being the major component and MoO_3- and MoO_2-type oxides being the minority species. Fig. 15B contains two plots of the laterally

resolved Raman spectra recorded of this sample. The Raman image a of Fig. 15B shows the intensity distribution of the band at 750 cm^{-1} characteristic of MoO_2-type oxides, while the Raman image b of Fig. 15B shows the intensity distribution of the band at 850 cm^{-1} characteristic of Mo_5O_{14}-type oxide. The different intensity distributions obtained for the two characteristic metal–oxygen vibrations evidence that the sample is structurally heterogeneous. Areas showing a high intensity of the Mo_5O_{14} band at 850 cm^{-1} exhibits only weak band intensities due to MoO_2 and vice versa. Thus, it may be concluded that the Mo_5O_{14}-type and MoO_2-type mixed oxides are mutually formed. This result is in agreement with the observation of a spatially heterogeneous element distribution as determined by EDX (see Section 3.1).

4. Conclusions

Catalytic tests showed that activation at 813 K in inert gas resulted in an increase of the catalytic methanol oxidation and a CH_2O yield by 300%. The activation energies of the formaldehyde formation were found to be similar for both catalysts. Therefore, it can be suggested that the reaction mechanism of the formaldehyde formation was not altered by the thermal activation as compared to the reaction over the precursor oxide. On the other hand, the pre-exponential factors as determined from the Arrhenius plots differed significantly. This result suggests a higher concentration of sites active for the formaldehyde formation on the thermally activated catalyst as compared to the untreated mixed oxide. Because thermal activation may have caused the formation of surface oxygen defects, there is reason for the assumption that these defects play the key role for the improved catalytic activity as often stated in the literature [3–6,54].

In order to understand this increase of the catalytic reactivity of an MoVW mixed oxide catalyst, the compositional changes were investigated which occur during the activation. SEM–EDX of the untreated catalyst revealed at least two different phases of different V concentrations. The sample had a homogeneous element distribution at the smaller length scale according TEM–EDX. While TEM detected only traces of small crystallites in the pristine oxide, pointing to a beginning crystallization of Mo_5O_{14}-type oxide, the inert activation led to crystallization. Nanometer sized crystals of MoO_3-type structure and even larger crystals with Mo_5O_{14}-type structure were detected. However, a fraction of the sample still remained amorphous as revealed by TEM. According to SEM–EDX and TEM–EDX, the thermally activated mixed oxide exhibited an inhomogeneous element distribution in the micron and submicron regime.

RBS, XPS, ISS and UPS gave the analytical confirmation that the thermally activated catalyst contained less bulk and surface oxygen and, hence, more oxygen defects relative to the untreated precursor oxide. The combination of these methods was necessary to show that this holds true for both the surface region and the bulk. A picture of the bulk composition and stoichiometry was developed by RBS, RFA, global EDX and XRD. The comparison of the XPS and RBS data, on the other hand, revealed that the degree of surface reduction cannot be determined precisely enough by XPS. The combined data can be rationalized in terms of a core–shell model of the activated catalyst, as shown in Scheme 4, the core being mostly of Mo_5O_{14}-type oxides, and the shell having a higher degree of reduction and an unknown structure. The core and the shell may act differently in the catalytic process. While the shell provides a high number of active sites and allows fast surface oxygen diffusion, the core may act as the electron-accepting reservoir due to its high electronic conductivity.

XPS evidenced that the oxygen depletion influences mainly the oxidation states of Mo and V. In line with the literature [30,73], W may be considered as a structural promotor. A distinguished Mo^{4+} state appeared upon thermal activation and the concentration of V^{4+} increased relative to V^{5+}. In addition, thermal activation led to a depletion of V in the surface-near region by phase separation as shown by comparison of the XPS and ISS results with the EDX mappings. Catalysis under higher oxygen partial pressures led to an increase of the surface V concentration. These observations of changing surface V concentrations may be interpreted by gas phase dependent bulk segregation and redispersion

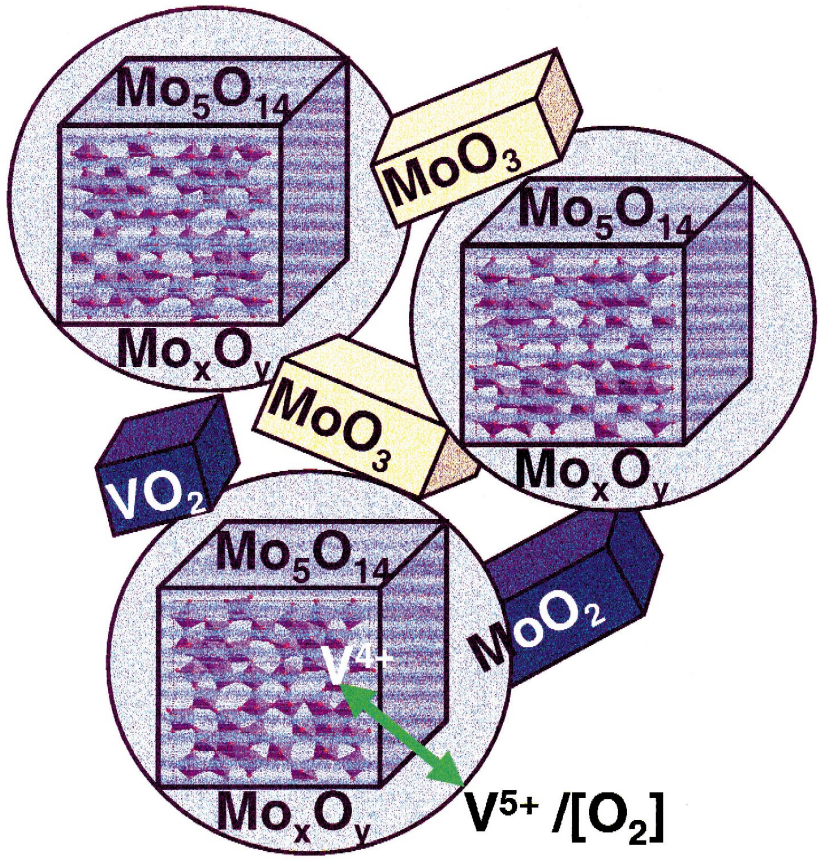

Scheme 4. Schematic drawing of the proposed core–shell model of MoVW mixed oxide catalysts.

(spreading) of the oxidic surface phase with a high V content. Hence, vanadium migrates between core and shell (XPS/ISS) and it segregates into separate phases (EDX) depending on its degree of reduction. UPS showed changes of the valence band confirming redox and structural alterations of the surface near regions upon thermal activation. Hence, the core shell model has to be extended to different phases present at the same time with different bulk and surface structure and stoichiometry (Scheme 4).

XRD characterization of the starting material showed the presence of a nanocrystalline material in line with the SEM/TEM investigations. The XRD pattern of the untreated starting material can be simulated and interpreted as being a mixture of nanocrystalline Mo_5O_{14}-type and MoO_3-type oxides. Confocal Raman microspectroscopy confirmed the presence of two different components in the starting mixed oxide and the spectra were assigned accordingly. After thermal activation, the mixed oxide consisted of a mixture of a majority of Mo_5O_{14}-type and a minority of crystalline MoO_3-type oxides. The presence of traces of MoO_2-type and VO_2-type oxides cannot be ruled out by XRD. The Raman spectrum of the major Mo_5O_{14}-type phase could be identified by statistical data evaluation and by comparison with the XRD result. Raman microscopy confirmed the presence of small amounts of MoO_3-type and MoO_2-type oxides. This result may be understood in relation to the metastability of Mo_5O_{14} with respect to MoO_3 and MoO_2 at its formation temperature [16,44]. The combined positive XRD

and Raman identification of the Mo_5O_{14}-type oxide as the majority component may be related to the observed increase of the catalytic activity for formaldehyde formation by a factor of 3 after thermal activation. These combined observations strongly suggest that the Mo_5O_{14}-type oxide is one relevant candidate for the core structure of the MoVW phase being active and selective for selective partial oxidation reactions (Scheme 4).

Andrushkevich [30] reported on a high activity and selectivity of Mo_4O_{11} for the partial oxidation of acrolein. This observation is highly interesting with respect to the presented results. Mo_4O_{11} has an oxygen stoichiometry of 2.75 being very close to the one of Mo_5O_{14}, with 2.8. Despite this close stoichiometry, both crystal structures are very different as shown in Scheme 3. It is known from experiments to synthesize single phase, well-crystallized Mo oxides that Mo_4O_{11} exhibits a local stability maximum in the phase regime between MoO_2 and MoO_3 [69]. The local stability maximum of Mo_4O_{11} and the metastability of Mo_5O_{14} may explain the difference in the reported observations and those of Andrushkevich [30]. Due to the high thermodynamic stability of Mo_4O_{11}, which can coexist with the catalytically inactive MoO_2, however, Mo_5O_{14} may be regarded as being more active than Mo_4O_{11}. The Mo_5O_{14}-type oxide remains nanocrystalline under the preparation conditions usually used. This thermodynamically highly unstable oxide and its high instability (high internal energy) is seen to be responsible for a high catalytic activity. Cation ($V^{5+/4+}$) and anion diffusion may be easy and fast redox changes within the structure may be possible. Hyde and O'Keefe [53] developed a general understanding of a cylindrical shear mechanism which relates Mo_5O_{14}, $Mo_{17}O_{47}$, $W_{18}O_{49}$, $Nb_{16}W_{18}O_{94}$, $Bi_6Nb_{34}O_{94}$, and tetragonal tungsten bronzes. According to this mechanism, the rotation of an Mo_4O_{20}-subunit within the MoO_3-derived oxide planes leads to the formation of sevenfold, and four-fold coordination beside the six-fold coordination, primarily without any change in stoichiometry or the oxidation state of the metal centers. This rotational shear mechanism can occur at any site within the molybdenum oxide layer, thus, leading to broad varieties of possible defect structures, superstructures, intergrowth and nonstoichiometries. This model explains the structure of the investigated MoVW mixed oxide. It is nanocrystalline and of the Mo_5O_{14}-type structure. In addition, the metastability of Mo_5O_{14} with respect to its disproportionation into MoO_2 and MoO_3 may shed light into the observed long-time instability of these types of industrial catalysts.

Mo_5O_{14}, as Mo_4O_{11}, tolerates the incorporation of considerable amounts of V and W [47]. Thus, mixed MoVW oxides are formed from MoO_3, WO_3, and V_2O_5 at high temperatures with crystal structures resembling that of Mo_5O_{14} [45–47]. The stoichiometry of such phases were reported to be $(Mo_{0.92}V_{0.08})O_{14}$ or $(Mo_{0.75}W_{0.25})O_{14}$) [21], respectively. The incorporation of W, especially, seems to favor the formation of Mo_5O_{14}-type oxides and can be compared with the results on Ta and Nb incorporation [44,48]. Hence, it may be concluded that the incorporation of about 8 at.% W into the investigated mixed Mo_5O_{14}-type oxide leads to its stabilization. This suggestion also seems to be supported by the observation of a homogeneous W distribution throughout the MoVW oxide at all length scales investigated irrespective of the thermal treatment. Vanadium is statistically incorporated into Mo_5O_{14} [45,46], although it seems to prefer octahedral sites close to a metal–metal bond ($Mo^{5+/4+}$ centers) in the structurally related $Mo_{17}O_{47}$ [12]. In addition, Mo_5O_{14} seems to tolerate large variations in the V content up to 30 at.%. This fact explains why mainly Mo_5O_{14}-type oxides were detected by XRD and Raman, although SEM– and TEM–EDX revealed large variations in the V distribution.

In summary, $(MoVW)_5O_{14}$-type oxides are promising candidates for the active and selective phase in partial oxidation reactions. These $(MoVW)_5O_{14}$-type oxides are complex systems containing several minority species besides the Mo_5O_{14}-type phase, which is highly variable in its chemical composition and oxidation state depending on the redox potential of the surrounding gas phase. The discussed results of the physicochemical characterization additionally revealed that the chemical bulk and surface composition of this Mo_5O_{14}-type oxide varies with thermal activation and oxygen potential. A core–shell model is suggested to describe the active catalyst state, the shell providing a high number of active centers, the core high electronic conductivity and ion mobility.

Acknowledgements

This work was financially supported by the BMBF through its catalysis program (BMBF-Vorhaben 03D0058B).

References

[1] R.K. Grasselli, Catal. Today 49 (1999) 141.
[2] P. Mars, D.W. van Krevelen, Chem. Eng. Sci. 3 (1954) 41, Special Suppl.
[3] K. Brückman, R. Grabowski, J. Haber, A. Mazurkiewicz, J. Slocynski, T. Wiltowski, J. Catal. 104 (1987) 71.
[4] A.B. Anderson, D.W. Ewing, Y. Kim, R.K. Grasselli, J.D. Durrington, J.F. Brazdil, J. Catal. 96 (1985) 222.
[5] A.R. Adams, T.J. Jennings, J. Catal. 3 (1964) 549.
[6] J. Haber, in: G. Ertl, H. Knözinger, J. Weitkamp (Eds.), Handbook of Heterogeneous Catalysis vol. 5 Wiley-VCh, Weinheim, 1997, p. 2253ff.
[7] G. Hägg, A. Magnéli, Ark. Kemi 19 (1944) 1.
[8] A. Magnéli, Acta Chem. Scand. 2 (1948) 501.
[9] A. Magnéli, Acta Chem. Scand. 2 (1948) 861.
[10] A. Magnéli, Acta Crystallogr. 6 (1953) 495.
[11] L. Kihlborg, A. Magnéli, Acta Chem. Scand. 9 (1955) 471.
[12] L. Kihlborg, Acta Chem. Scand. 13 (1959) 954.
[13] L. Kihlborg, Acta Chem. Scand. 14 (1960) 1612.
[14] L. Kihlborg, Acta Chem. Scand. 17 (1963) 1485.
[15] L. Kihlborg, Ark. Kemi 21 (1963) 365.
[16] L. Kihlborg, Ark. Kemi 21 (1963) 427.
[17] L. Kihlborg, Ark. Kemi 21 (1963) 443.
[18] L. Kihlborg, Ark. Kemi 21 (1963) 461.
[19] L. Kihlborg, Ark. Kemi 21 (1963) 471.
[20] S. Åsbrink, L. Kihlborg, Acta Chem. Scand. 18 (1964) 1571.
[21] P.F. Cornaz, J.H.C. van Hooff, F.J. Plujim, G.C.A. Schuit, Discuss. Faraday Soc. 41 (1966) 290.
[22] L.A. Bursill, Acta Crystallogr. A28 (1972) 187.
[23] H. Guyot, E. Al Khoury, J. Marcus, C. Schlenker, M. Banville, S. Jandl, Solid State Commun. 79 (1991) 307.
[24] L. Kihlborg, Ark. Kemi 21 (1963) 357.
[25] N.N. Greenwood, Ionic Crystals, Lattice Defects and Nonstoichiometry, Butterworth, London, 1968.
[26] O. Nakamura, T. Kodama, I. Ogino, Y. Miyake, Chem. Lett. (1979) 17.
[27] P.L. Gai, W. Thoeni, P.B. Hirsch, J. Less-Common Met. 54 (1979) 263.
[28] P.L. Gay-Boyes, J. Solid State Chem. 104 (1993) 119.
[29] C.A. Catlow, in: O.T. Sorensen (Ed.), Nonstoichiometric Oxides, Academic Press, 1981.
[30] T.V. Andrushkevich, Kinet. Catal. 38 (1997) 289.
[31] T.G. Kuznetsova, G.K. Boreskov, T.V. Andrushkevich, React. Kinet. Catal. Lett. 12 (1979) 531.
[32] T.V. Andrushkevich, L.M. Plyasova, T.G. Kuzetsova, React. Kinet. Catal. Lett. 12 (1979) 463.
[33] J. Tichy, J. Kusta, J. Venkl, Collect. Czech. Chem. Commun. 39 (1974) 1797.
[34] V.C. Malshe, S.B. Chandalia, J. Appl. Chem. Biotechnol. 27 (1977) 575.
[35] R.K. Grasselli, J.D. Burrington, Adv. Catal. 30 (1981) 133.
[36] J. Tichy, J. Kusta, J. Machek, Collect. Czech. Chem. Commun. (1982) 698.
[37] M. Ai, Appl. Catal. 27 (1986) 167.
[38] L.M. Plyasova, L.P. Solov'eva, G.N. Kryukova, T.V. Andrushkevich, Kinet. Catal. 31 (1990) 1253.
[39] T.V. Andrushkevich, V.M. Bondareva, G.Y. Popova, L.M. Plyasova, Stud. Surf. Sci. Catal. 72 (1992) 91.
[40] T.V. Andrushkevich, V.M. Bondareva, G.Ya. Popova, L.M. Plyasova, in: P. Ruiz, B. Delmon (Eds.), Surface Science and Catalysis: New Developments in Selective Oxidation by Heterogeneous Catalysis vol. 72 Elsevier, Amsterdam, 1992, p. 91.
[41] T.V. Andrushkevich, Catal. Rev. — Sci. Eng. 35 (1993) 213.
[42] S. Breiter, M. Estenfelder, H.-G. Lintz, A. Tenten, H. Hibst, Appl. Catal. A 134 (1996) 81.
[43] H. Werner, O. Timpe, D. Herein, Y. Uchida, N. Pfaender, U. Wild, R. Schlögl, H. Hibst, Catal. Lett. 44 (1997) 153.
[44] N. Yamazoe, L. Kihlborg, Acta Cryst., B 31 (1975) 1666.
[45] T. Ekström, M. Nygren, Acta Chem. Scand. 26 (1972) 1827.
[46] T. Ekström, Acta Chem. Scand. 26 (1972) 3381.
[47] L. Kihlborg, Acta Chem. Scand. 23 (1969) 1834.
[48] T. Ekström, M. Nygren, Acta Chem. Scand. 26 (1972) 1836.
[49] T. Ekström, Acta. Chem. Scand. 26 (1972) 1843.
[50] T. Ekström, Mater. Res. Bull. 7 (1972) 19.
[51] L. Kihlborg, Acta. Chem. Scand. 14 (1962) 1612.
[52] A. Magnéli, Ark. Kemi 1 (1949) 223.
[53] B.G. Hyde, M. O'Keefe, Acta Cryst., A 29 (1973) 243.
[54] M. Niwa, M. Mizutani, M. Takahashi, Y. Murakami, J. Catal. 70 (1981) 14.
[55] F. Trifiro, I. Pasquon, J. Catal. 12 (1968) 412.
[56] J. Guidot, J.E. Germain, React. Kinet. Catal. Lett. 15 (1980) 389.
[57] T. Wadayama, T. Saito, W. Suetaka, Appl. Surf. Sci. 20 (1984) 199.
[58] J.S. Chung, R. Miranda, C.O. Bennett, J. Catal. 114 (1988) 398.
[59] H. Adkins, W.R. Peterson, J. Am. Chem. Soc. 53 (1931) 152.
[60] C.J. Machiels, A.W. Sleight, in: H.F. Barry, P.C.H. Mitchell (Eds.), Proc. 4th Intern. Conf. on the Chemical Uses of Molybdenum, Climax Molybdenum, Ann Arbor, 1982, p. 411.
[61] G. Mestl, P. Ruiz, B. Delmon, H. Knözinger, J. Phys. Chem. 98 (1994) 11269.
[62] M. Mayer, SIMNRA User's Guide, Report IPP 9/113, Max-Planck-Institut für Plasmaphysik, Garching, 1997.
[63] K. DeBraekeleer, D.L. Massart, Chemom. Intell. Lab. Syst. 39 (1997) 127.
[64] M. Kraus, in: G. Ertl, H. Knözinger, J. Weitkamp (Eds.), Handbook of Heterogeneous Catalysis vol. 5 Wiley-VCh, Weinheim, 1997, p. 2159.
[65] M. Dieterle, G. Mestl, J. Jäger, Y. Uchida, R. Schlögl, in preparation.

[66] J.M. Aigler, V.B. Kazansky, M. Houalla, A. Proctor, D.M. Hercules, J. Phys. Chem. 99 (1995) 11489.
[67] W. Grünert, A.Yu. Stakheev, R. Feldhaus, K. Anders, E.S. Shpiro, K.M. Minachev, J. Phys. Chem. 95 (1991) 1323.
[68] J. Mendialdua, R. Casanova, Y. Barbeaux, J. Electron Spectrosc. Relat. Phenom. 71 (1995) 49.
[69] A. Blume, G. Mestl, in press.
[70] M. Dieterle, G. Mestl, in press.
[71] K. Hermann, M. Witko, R. Druzinic, A. Chakrabarti, B. Tepper, M. Elsner, A. Gorschlüter, H. Kuhlenbeck, H.J. Freund, J. Electron Spectrosc. Relat. Phenom. 98/99 (1999) 245.
[72] R. Tokarz, K. Hermann, A. Blume, U. Wild, D. Frickel, G. Mestl, A. Knop-Gerike, R. Schlögl, in press.
[73] C. Bauer, Y. Koyasu, S. Nakamura, O. Kitao, J. Mol. Struct.: THEOCHEM 461 (1999) 291.